High Intensity Femtosecond Enhancement Cavities

by

Gilberto Abram

B.S., E.E.C.S., Massachusetts Institute of Technology (2008)
B.S., Physics, Massachusetts Institute of Technology (2008)

Submitted to the Department of Electrical Engineering
and Computer Science
in partial fulfillment of the requirements for the degree of

Master of Engineering in Electrical Engineering and Computer Science

at the

MASSACHUSETTS INSTITUTE OF TECHNOLOGY

June 2009

ARCHIVES

© Massachusetts Institute of Technology 2009. All rights reserved.

MASSACHUSETTS INSTITUTE OF TECHNOLOGY
AUG 24 2010
LIBRARIES

Author .....
Department of Electrical Engineering and Computer Science
May 22, 2009

Certified by .....
Franz X. Kärtner
Professor of Electrical Engineering
Thesis Supervisor

Accepted by .....
Arthur C. Smith
Professor of Electrical Engineering
Chairman, Department Committee on Graduate Theses

High Intensity Femtosecond Enhancement Cavities

by

Gilberto Abram

Submitted to the Department of Electrical Engineering and Computer Science
on May 22, 2009, in partial fulfillment of the
requirements for the degree of
Master of Engineering in Electrical Engineering and Computer Science

Abstract

To produce extreme ultraviolet radiation via high harmonic generation (HHG) in rare gases, light intensities in excess of 10^{14} W/cm^2 are required. Usually such high intensity are obtained by parametric amplification of laser pulses, which in turn reduces the pulse repetition rate to a few kHz. Given that the HHG process is inherently inefficient, with conversion ratios less than 10^{-5}, only a small fraction of the pulse energy is lost in the nonlinear interactions, so it is possible to enhance the pulse intensity in a passive cavity retaining the original repetition rate. I present here a novel broadband resonator design which has the potential of supporting intracavity intensities in excess of 10^{15} W/cm^2 while allowing the harmonic radiation to couple out of the cavity with no loss. Extensive computer simulations are performed with a custom software package, and the required mirrors have been constructed using a standard microfabrication process.

Thesis Supervisor: Franz X. Kärtner
Title: Professor of Electrical Engineering

Acknowledgments

I would like first of all to thank Professor Franz Kärtner for giving me the opportunity to work with his group towards this degree. Not only he has been a terrific supervisor during this past year, but also an invaluable mentor since my first undergraduate research experience.

Thanks to the entire Optics and Quantum Electronics group at RLE for all the help that I received, and in particular Jonathan Birge and Edilson Falcão-Filho who sacrificed a lot of their time at the beginning of the project to help me.

I am much indebted to Trey Holzwarth and Billy Putnam for their help with the fabrication process for the cavity mirrors.

Finally, I want to thank my parents Ermanno and Mariagrazia, my brother Gianluca, Amanda, and all of my family and friends that always supported me.

Contents

1 Introduction **13**

2 Background **19**

2.1 Wave optics 19

2.1.1 Scalar wave equation 20

2.1.2 Fourier decomposition into monochromatic fields 21

2.1.3 Wavefront decomposition in terms of plane wave solutions . . 22

2.1.4 Wave propagation in the spatial frequency domain 25

2.1.5 Evanescent waves 27

2.1.6 Effects of thin optical elements on wavefronts 28

2.1.7 Paraxial approximation 28

2.2 Two mirror resonators 29

2.2.1 Longitudinal resonance 30

2.2.2 Transverse resonance 31

2.3 Phase of the atomic polarization during HHG 32

3 Mathematical theory behind the numerical simulator **35**

3.1 Finite discrete description of wavefronts and linear optical elements . 36

3.2 The quasi-discrete Hankel transform 39

3.3 Simulation of thin optical elements 41

3.3.1 Hard apertures, partially transmitting elements and phase masks 42

3.3.2 Thin lenses 43

3.3.3 Mirrors 44

3.4 Linear optical systems 46
3.4.1 Scattering matrices 46
3.4.2 Transfer matrix composition technique 48
3.4.3 Direct composition of S-matrices 49
3.4.4 Physical interpretation of the composition of scattering matrices 51
3.4.5 Finding eigenmodes 53

4 Design and analysis of the cavity **55**
4.1 Choice of using a confocal cavity 55
4.2 Single-mode operation 59
4.2.1 Single mode operation in a degenerate cavity 60
4.2.2 Traditional ways of limiting degeneracy 62
4.2.3 Restriction of the mirror size 63
4.2.4 Structure of the two dominant modes 69
4.3 Analysis of the focus 71
4.4 Coupling of external fields 77
4.5 Phase matching 81

5 Experimental work **87**
5.1 Fabrication of the mirrors 87
5.2 Monochromatic cavity stabilization 88

6 Conclusions **91**

List of Figures

2-1 For a plane wave in two dimensions, each linear cross section is sinusoidal. Given that $|\boldsymbol{k}|$ is constant, $\boldsymbol{k}$ (and in particular k_z) can be found from k_x. 25

2-2 Multipass interference inside a Fabry-Perot resonator. 30

2-3 Phase of the atomic polarization for a single neon atom at the 45th harmonic of a 825 nm driving field, from [1]. 33

3-1 A resonant wavefront undergoes a roundtrip of the cavity without altering its spatial pattern, up to a multiplicative constant. 38

3-2 Effect of a hard aperture on wavefronts. 42

3-3 Calculation of the matrix representation of a thin lens. 43

3-4 Calculation of the matrix representation of a mirror. 45

3-5 Wavefronts naming conventions with scattering matrices. 46

3-6 Wavefront naming convention for composition of S-matrices. 50

3-7 Roundtrip transformation of a wavefront in a system. 53

4-1 Fraction of the energy left after one cavity roundtrip for the least lossy resonant mode as the distance between the mirrors is varied. 56

4-2 Mode selectivity when an iris is placed at the center of the cavity. . . 62

4-3 Mode selectivity obtained by displacing the mirrors from confocal configuration. 63

4-4 Naming of the variables determining the geometry of the cavity. . . . 64

4-5 Mode selectivity obtained by varying the extent of the mirror surface, shaped as a circular ring. 65

4-6 Single mode cavity as λ is varied. (a) Δr to achieve single mode operation (together with the analytic expression), (b) roundtrip losses of the second mode. 66
4-7 Single mode cavity as R is varied. (a) Δr to achieve single mode operation (together with the analytic expression), (b) roundtrip losses of the second mode. 67
4-8 Single mode cavity as r is varied. (a) Δr to achieve single mode operation (together with the analytic expression), (b) roundtrip losses of the second mode. 68
4-9 Magnitude of the complex field of the first mode (u_1). 69
4-10 Magnitude of the complex field of the second mode (u_2). 70
4-11 In phase addition of the first two modes (ψ_1). 70
4-12 Out of phase addition of the first two modes (ψ_2). 71
4-13 Direction of wave propagation for ψ_2. 72
4-14 Calculation of the size of the region of focus. 73
4-15 Field strength at the focus. 73
4-16 (a) gain and (b) spot size dependence on λ, together with the analytic expressions. 75
4-17 (a) gain and (b) spot size dependence on R, together with the analytic expressions. 75
4-18 (a) gain and (b) spot size dependence on r, together with the analytic expressions. 76
4-19 Proposed coupling scheme, using an axicon. 77
4-20 Angle of ring-shaped beam. 78
4-21 Beam angles in refraction from the mirror's substrate. 79
4-22 Field strength in both directions for the cavity and the coupling optics. 80
4-23 Plot of the total power and peak intensity in the forward and backward propagating waves. 81
4-24 Guoy phase shift calculated numerically. 82
4-25 Ponderomotive energy in normalized atomic units. 83

4-26 Total phase shift for the 101^{st} harmonic. 84
4-27 Total phase shift for the 281^{st} harmonic. 84

5-1 Etched mirror. 88
5-2 Pictures of the $LG_{0,0}$ to $LG_{9,0}$ and $LG_{12,0}$ modes. 90

Chapter 1

Introduction

Less than a year after the report of the implementation of the very first laser system, researchers demonstrated experimentally second harmonic generation ([2]) as predicted by nonlinear polarization theories, and opened the door for nonlinear optics. The key for this breakthrough was that for the first time it was possible to create very high, coherent electric fields which produced measurable nonlinear excitations.

This first experiments focused the light beam in a material to reach intensities on the order of 10^7 W/cm^2. As pulsed laser technology progressed, faster pulses allowed for reaching higher peak intensities and hence excite even the weaker higher order nonlinearities. One characteristic of perturbative nonlinearities is that in general higher order effects require higher intensities to produce the same output power. So, in a medium with inversion symmetry for example, we expect that at a given driving intensity the third harmonic will have more energy than the fifth, which in turn will have more energy than the seventh, and so on. Usually the output powers differ by a few orders of magnitudes, so we would expect to be able to observe only the first few harmonics.

In the late 1980s, however, an unexpected effect was discovered experimentally: at an intensity above 10^{13} W/cm^2, a laser pulse shined into a rare gas would produce very high harmonics ([3]). In the initial experiment, the 33rd harmonic of a 1064 nm driving pulse was measured. Since then, even higher harmonics have been generated, with wavelengths as short as a couple of nanometers. What distinguished high

harmonic generation (HHG) from other nonlinear processes was that it was not a perturbative effect: the intensity of the generated harmonics decayed with increasing frequency only initially, and was then fairly uniform up to a sharp cutoff.

The discovery of HHG attracted immediate interest in a number of fields, even before it was fully understood theoretically. It promised the generation of coherent extreme ultraviolet (EUV) radiation from a device with a cost and size small enough for a university laboratory. Such radiation source is of interest in spectroscopy and crystallography, and also for biological imaging due to the possibility to have a coherent source in the water window (the spectral region between 2.3 nm and 4.4 nm where imaging has the maximum contrast with respect to water). Furthermore, the broad bandwidth of the produced harmonics stirred up the ultrafast optics community because it provided the means to generate light pulses lasting only a few tens of attoseconds (1 as= 10^{-18} s)[1]. Such pulses could allow for imaging with time resolution near the atomic time unit and sub-atomic spatial resolution. In the industry, semiconductor manufacturers saw HHG as a promising EUV source for the future 13.5 nm lithography technology.

While research in the field is still very active, there have been some important results such as the creation of isolated, sub 100 as pulses ([4]) and the tomographic imaging of one of the molecular orbitals of N_2 ([5]).

One of the current limitations of HHG is that the achievable repetition rate is extremely low (a few kHz) due to the fact that the high pulse energies required to excite the process are not available directly from the driving laser, requiring an additional amplification stage which can operate at a pulse rate much lower than the hundreds of MHz of a mode-locked laser. Furthermore, the conversion efficiency to the harmonics is extremely low, between 10^{-5} in optimal cases and 10^{-8} or less to generate the highest harmonics; in other words, the energy content of the initial laser pulse is basically undepleted, and it is ultimately wasted.

A similar problem occurs with most nonlinear processes, for example in second

[1]Pulses generated from mode-locked lasers are limited by the bandwidth of the gain medium to about 5 fs of duration or more.

harmonic generation (SHG). In that case, the intensity conversion efficiency increases as the square of the input intensity (in the low depletion limit). While reaching high instantaneous intensities is not too difficult with pulsed lasers, low efficiency can be a problem if we desire a CW output. An elegant solution was presented in [6]: a passive cavity enhanced the intensity of the laser by confining the input beam and making it interfere constructively with itself, and the nonlinear material was placed where the intensity was maximum. Not only the higher intensity in the cavity resulted in better conversion efficiency, but also the large fraction of the light that is not converted to the second harmonic keeps on circulating in the cavity, not going to waste but contributing to the nonlinear process during the next pass. In their initial experiment, a simple plano-concave cavity increased the second harmonic output power by a factor of 10. Nowadays, by refinement of the technique, second harmonic generation can be obtained with very high overall efficiencies even from low power CW lasers[2], basically limited only by absorption and other losses and not by the low conversion efficiency.

The use of a passive enhancement cavity in the case of HHG seems ideal: the intensity enhancement allows for use without amplification, retaining the high pulse repetition rate of the driving laser, and the confinement of the pulses allows for reusing a large fraction of the undepleted energy for the successive passes, increasing the conversion efficiency. However, there are a series of difficulties specific to HHG. The intensities required in the region where the rare gas is present are at least 10^{13} W/cm^2, and ideally up to about 10^{15} W/cm^2 or slightly above it[3], while the surface of a dielectric mirror can withstand peak intensities of about 10^{12} W/cm^2. If we want to generate harmonics efficiently, the intensity in the middle of the cavity needs to be 2-3 orders of magnitude higher than at the surface of the mirrors; using a tightly focusing cavity is not a desirable option because the mirrors will be located at the edge of stability, and also because the rapidly changing phase at the focus limits the length

[2]For example, green laser pointers output light at 532 nm obtained by SHG from 1064 nm radiation.

[3]For much higher intensities, the gas stays permanently in an ionized state and harmonic generation comes to a stop, and also the effects of the strong magnetic field prevent the unionized atoms to radiate efficiently.

over which HHG can occur without being limited severly by phase mismatch([1]).

A second problem is extracting the EUV radiation from the cavity where it is generated. Early attempts using an intracavity block of sapphire worked at the price of a reduced finesse of the cavity (therefore reducing the enhancement factor), and were described in [7]. The coupling efficiency obtained was under 10%, and the overall efficiencies reported were low. The state of the art coupling via intracavity elements was reported in [8], where a grating etched on a mirror is used to deviate the harmonics out of the cavity. The advantage of this setup is that it does not impact substantially the cavity enhancement, but on the other hand it still has coupling efficiencies under 10% and the harmonic frequencies are separated spatially by the grating, making the system not suitable for pulse generation. Furthermore, absorption of short wavelength radiation by most materials limits substantially the maximum order of the harmonic that can be coupled out of the cavity.

Another proposed coupling technique was that of creating a small hole in one of the cavity mirrors ([9]). The idea was that the hole should have been small enough to only perturb the cavity slightly, but the harmonics would couple out since, due to their shorter wavelength, they diffract less by the time they reach the mirror, so they would overlap maximally with the hole. Simulation results pointed at how a very small aperture can keep losses low, but increasing the size to a fraction of the mode waist would result in increased losses and poorer coupling of the driving pulse.

In this thesis, I propose a new design for a passive enhancement cavity geared towards high harmonic generation. It uses mirrors with large apertures to obtain a coupling efficiency of the harmonic radiation of practically 100%. It is not based on a slight perturbation of a common resonator, but rather on a different idea which can achieve low loss, high intensity gain from the mirror surface to the focus, practically single-mode operation, and a mode shape which offers good phase matching and a long interaction length for the nonlinear process.

In the next chapter I will review the basic mathematics of wave optics and paraxial resonators, together with the properties of HHG that are needed to calculate how well the process is phase-matched. The successive chapter describes in detail the mathe-

matical underpinnings of a fast MATLAB library that I developed for the numerical simulation of general optical systems in the wave optics paraxial approximation, able to simulate multiple internal reflections and to calculate the eigenmodes of a cavity. The library was used extensively in the design and analysis of the proposed resonator, which are the subject of the subsequent chapter. Finally, I will report on the results of the fabrication of the particular mirrors needed for a test CW cavity and on a feedback stabilization scheme for it.

The results of the simulations are very promising with regard to the possibility of using the cavity developed here to generate EUV with high efficiency. Furthermore, the simulation techniques and the software can be readily applied to the study of other systems.

Chapter 2

Background

The goal of this study is to design an optical resonator, which is composed by two or more mirrors separated by free space. While in principle Maxwell's equations could be solved for a laser pulse between the mirrors, this approach is computationally intractable due to the large size of the cavity compared to the wavelength and to the pulse width. Furthermore, blindly solving the equations will be of no help in the design process. It makes sense then to work within a simplified and more tractable framework that still captures all the details of interest.

Wave optics provides an adequate description of the phenomena involved in a typical cavity, while having the advantage of being much simpler to deal with conceptually and in computer code. In this section I will present a brief review of the key concepts of wave optics that will be used for the numerical simulations, together with some key results about the shape and spacing of the modes of a cavity made with spherical mirrors using the paraxial wave equation. Finally, I will show what is known about the phase of the atomic polarization during the HHG process, which will be crucial for phase-matching calculations.

2.1 Wave optics

In the context of wave optics, light is treated as a scalar wave, so phenomena involving diffraction and interference can be described effectively. In the case of a cavity, we are

interested mainly in the effects of diffraction as the light propagates from a mirror to the next one, and in the action of the mirrors on the propagating light. The derivations presented in this chapter are adapted from [10] and [11].

2.1.1 Scalar wave equation

It can be shown that in the case of a infinite extent medium without free charge and with spatially uniform permeability[1] and permittivity, the following quantities satisfy the wave equation[2]:

- the electric field $\mathbf{E}$,
- the magnetic field $\mathbf{H}$,
- the scalar potential Φ,
- the vector potential $\mathbf{A}$.

In the case of the three vector fields, the wave equation is obeyed independently by the component of the field in any direction, in particular for the three directions of a rectangular coordinate basis. For example the vector potential will satisfy the equation

$$\nabla^2 \mathbf{A} = \mu_0 \epsilon \frac{\partial^2 \mathbf{A}}{\partial t^2}, \tag{2.1}$$

where the speed of propagation is $c = 1/\sqrt{\mu_0 \epsilon}$. The same equation is satisfied by the other quantities.

A solution of Maxwell's equations in such a medium necessarily solves the wave equation for the quantities listed above[3], however the converse is not always the case. It is the case for the scalar potential and for the vector potential. It is not the case for

[1] It is assumed that all the materials that will be used are non magnetic, so $\mu \approx \mu_0$.

[2] Assuming that the divergence of $\boldsymbol{A}$ is chosen using the *Lorentz gauge*, giving

$$\boldsymbol{\nabla} \cdot \boldsymbol{A} + \mu_0 \epsilon \frac{\partial \Phi}{\partial t} = 0.$$

This choice of gauge is assumed in the rest of this work.

[3] This is true only because there are no free charges and ϵ is constant, giving $\boldsymbol{\nabla} \cdot \mathbf{E} = 0$, together with the fact that there are no boundaries, so no static or quasi-static fields can exist.

the electric and magnetic field though, since they need to be also divergence free to satisfy Maxwell's equations, which implies that there must be a certain relationship between the field components.

Since the ultimate objective is to be able to use a scalar wave equation to describe optical phenomena, dealing with the electric or magnetic field poses a problem. The vector potential does not have this limitation however, so we can in fact force an arbitrary polarization upon it:

$$\mathbf{A}(\mathbf{r}) = \hat{\mathbf{n}} \cdot f(\mathbf{r}),$$

and reduce the vector wave equation 2.1 to the scalar wave equation

$$\nabla^2 f = \mu_0 \epsilon \frac{\partial^2 f}{\partial t^2}. \tag{2.2}$$

2.1.2 Fourier decomposition into monochromatic fields

Since equation 2.2 is linear and time-invariant, it is possible to express any solution, which represents the wave amplitude as a function of position and time, as a function of position and frequency. Transformation from time domain to frequency domain and vice versa can be achieved very easily via the Fourier transform and its inverse:

$$F(x, y, z, \omega) = \frac{1}{2\pi} \int_{-\infty}^{\infty} f(x, y, z, t) e^{-j\omega t} \, \mathrm{d}t,$$

$$F(x, y, z, t) = \int_{-\infty}^{\infty} F(x, y, z, \omega) e^{j\omega t} \, \mathrm{d}\omega.$$

The advantage of using the Fourier components instead of the time domain solution stems from the fact that complex exponentials are eigenfunctions of linear operators. In particular,

$$\frac{\mathrm{d}}{\mathrm{d}t} e^{st} = s \cdot e^{st}.$$

If we take $s = j\omega$, by assuming that the solution has an $e^{j\omega t}$ time dependence [4] , then

[4] By which we mean that the actual disturbance at time t equals the real part of $F(\omega)e^{j\omega t}$, since there are no imaginary fields.

the wave equation reduces to Helmholtz equation:

$$(\nabla^2 + \omega^2 \mu_0 \epsilon)\, F(x, y, z, \omega) = 0, \tag{2.3}$$

which is independently solved by each Fourier component.

By solving 2.3 for all frequencies, we also solved the wave equation 2.2 for all times, since the two solutions are related via the Fourier transform. Therefore the fact that we will need to use a pulsed laser in the cavity instead of a CW source makes no difference, as long as the resonator works well for all the frequency components of the pulse train and does not introduce temporal spreading due to dispersion. Since the dispersion can be calculated from the solutions in frequency domain, we can simply focus on solving for the cavity resonant modes in the monochromatic case. Later, the results for a range of frequencies can be combined to recover the time domain behavior.

If we denote the frequency of the monochromatic wave of interest by ω_0, then a one dimensional wave at that frequency will have a wavelength $\lambda_0 = 2\pi c/\omega_0$, and by using the dispersion relation in a uniform medium $k = \omega/c = 2\pi/\lambda$, we can drop any time dependence by introducing the scalar field $\psi(x, y, z) = \psi(\mathbf{r})$, which represents the complex solution to the Helmholtz equation (here in canonical form) at the frequency ω_0:

$$(\nabla^2 + k_0^2)\, \psi(\mathbf{r}) = 0, \tag{2.4}$$

where $k_0 = \omega_0/c = 2\pi/\lambda_0$ is the wavenumber.

2.1.3 Wavefront decomposition in terms of plane wave solutions

An important set of solutions for studying diffraction is that of plane waves, which can be described by a simple sinusoidal disturbance along their direction of propagation:

$$\psi(\mathbf{r}) = \Psi_0 \exp(-j\mathbf{k} \cdot \mathbf{r}).$$

The regions of constant phase for this solution are infinite-extent planes perpendicular to the vector $\mathbf{k}$, along which the disturbance propagates. If we assume $\mathbf{k} = k_0\hat{\boldsymbol{z}}$, then in time domain

$$f(x, y, z, t) = \Psi_0 \exp\left(j(\omega t - kz)\right).$$

Since there is nothing special about the z-axis in equation 2.4, but k_0 is fixed due to the fact that $\omega = \omega_0$ is constant, then the vector $\mathbf{k}$ in the more general solution has fixed magnitude but arbitrary direction. The set of solutions represents then the basic plane wave as above, rotated so that the direction of propagation points in every possible direction.

It is interesting to analyze the value of the spatial part of such a solution on a plane of constant z. With z being fixed, the disturbance on the plane can be described as a function of x and y only, $u_z(x, y) = \psi(x, y, z)$, and if we rewrite the wavevector as $\mathbf{k} = k_x\hat{\boldsymbol{x}} + k_y\hat{\boldsymbol{y}} + k_z\hat{\boldsymbol{z}}$, then for $z = 0$

$$u_0(x, y) = \Psi_0 \exp\left(-j(k_x x + k_y y)\right),$$

with the only limitation that $k_x^2 + k_y^2 \leq k_0^2$, since the magnitude of the wavevector is fixed.

The set of complex functions on the $z = 0$ plane is a subset with limited maximum spatial frequency of the complete Fourier basis of functions on the plane. A plane wave propagating in the direction perpendicular to the plane considered will always have uniform phase across the entire plane, therefore it constitutes the DC component. The highest spatial frequencies attainable on the cross sectional plane will be those of the plane waves propagating in a direction parallel to the plane itself, corresponding to a spatial frequency in the plane equal to the spatial frequency along the direction of propagation, which is k_0.

Assuming for now that $|\mathbf{k}|$ is larger than any of the spatial frequencies in the $z = 0$ plane, or in other words that the spatial variations of the disturbance $u_0(x, y)$ in the plane occur over distances much longer than the wavelength, it is possible to describe $u_0(x, y)$ as a superposition of plane waves in space.

The key mathematical concept is once again the Fourier transform, this time between the two dimensional space of the $z = 0$ plane described by spatial coordinates $\mathbf{r} = (x, y)$ and the space of plane waves in that plane, described by spatial frequencies $\boldsymbol{\nu} = (\nu_x, \nu_y)$[5]:

$$\mathcal{F}\{u(x,y)\} = U(\nu_x, \nu_y) = \iint u(x,y) \exp\left[-j2\pi(\nu_x x + \nu_y y)\right] \mathrm{d}x\mathrm{d}y, \tag{2.5}$$

$$\mathcal{F}^{-1}\{U(\nu_x, \nu_y)\} = u(x,y) = \iint U(\nu_x, \nu_y) \exp\left[j2\pi(\nu_x x + \nu_y y)\right] \mathrm{d}\nu_x\mathrm{d}\nu_y. \tag{2.6}$$

If the disturbance is known across the plane $z = 0$, then it is possible to express it as a weighted sum of two-dimensional plane waves, as in the inverse Fourier transform 2.6, where the weights are simply the Fourier coefficients found via the forward transform 2.5.

Each plane wave component in the x-y plane can be related to a plane wave in three dimensional space, since the constraint on k being constant implies

$$k_x^2 + k_y^2 + k_z^2 = k_0^2. \tag{2.7}$$

It is important to notice how $k_x = 2\pi\nu_x$ and $k_y = 2\pi\nu_y$ are known for a given Fourier component, so the absolute value of k_z is uniquely determined. The sign however is not determined, since both the plane wave with $\mathbf{k} = (k_x, k_y, k_z)$ and the plane wave with $\mathbf{k} = (k_x, k_y, -k_z)$ have the same value on the plane $z = 0$.

In general there is no way to resolve this degeneracy, unless some additional assumptions are made. A reasonable assumption when we study the diffraction pattern of a wave disturbance propagating mainly in a particular direction (along which we align the z-axis) is to restrict all the constituents plane waves to not have a component of their wavevector to point in the direction of negative z. So the wavevector's

[5]Or equivalently wavevectors, since $\mathbf{k} = 2\pi\boldsymbol{\nu}$ and so all the equations of interest are scaled by a multiplicative constant. It is common in Fourier optics to deal with spatial frequencies in the plane of interest, while plane waves in space are usually described in terms of their wave vector $\boldsymbol{k}$.

z-component is uniquely determined by the imposed condition $k_z > 0$:

$$k_z = \sqrt{k_0^2 - k_x^2 - k_y^2}. \tag{2.8}$$

2.1.4 Wave propagation in the spatial frequency domain

The general problem in wave propagation is to find a method that given the complex disturbance on the $z = 0$ plane allows us to calculate what the disturbance is on a plane $z = z_0$, for a generic $z_0 > 0$, without solving Helmholtz equation over the entire volume of interest.

In the case of a plane wave, the solution to the problem is trivial. Figure 2-1 depicts the situation for two dimensional waves. In this case there is a plane wave for which the magnitude of the wavevector is known. The cross section along any straight line parallel to the z-axis will be a sinusoidal oscillation with wavenumber k_z ($\lambda_z = 2\pi/k_z$), and if we look at the wavefront for $z > 0$, we see that each point on it undergoes a phase shift of $-2\pi z/\lambda_z$, so we can derive the equation for the propagation of the wavefront of a plane wave in two dimensions:

$$u_{z_0}(x) = u_0(x) \cdot \exp(-2\pi z_0/\lambda_z) = u_0(x) \cdot \exp(-z_0 k_z).$$

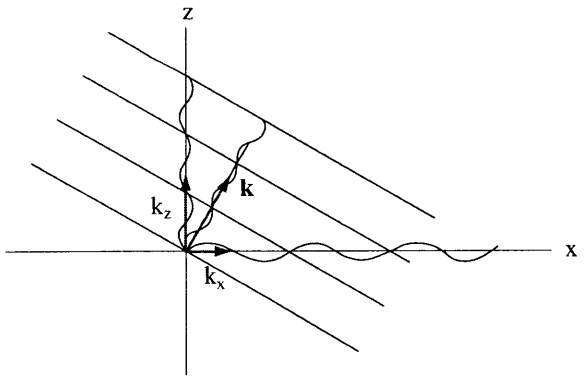

Figure 2-1: For a plane wave in two dimensions, each linear cross section is sinusoidal. Given that $|\boldsymbol{k}|$ is constant, $\boldsymbol{k}$ (and in particular k_z) can be found from k_x.

In practice though the only information that we are given is the cross section along the x-axis and the distance of propagation z_0. In the case of a plane wave, the cross section will look again as a sinusoidal oscillation whose wavenumber k_x we can determine. From there, k_z can be found and we can apply the above equation.

The case of a three dimensional plane wave is analogous (but harder to show pictorially): the wavefront on the x-y plane will be a plane wave of which we can determine directly k_x and k_y, from which k_z can be found using equation 2.8 and so the appropriate phase shift can be applied to find the new wavefront at $z = z_0$.

Being able to propagate a plane wave's wavefront means that any disturbance can be propagated due to the linearity of Helmholtz's equation. The phase shift of each Fourier component can be easily calculated:

$$U_{z_0}(\nu_x, \nu_y) = \exp\left(-jz_0\sqrt{k_0^2 - k_x^2 - k_y^2}\right) U_0(\nu_x, \nu_y) =$$

$$= \exp\left(-jk_0 z_0\sqrt{1 - (\lambda_0\nu_x)^2 - (\lambda_0\nu_y)^2}\right) U_0(\nu_x, \nu_y). \tag{2.9}$$

A linear operator that performs the phase shift for a given λ (or k) and z can then be defined as the linear operator $F_{\lambda,z}$ for which

$$U_{z_0}(\nu_x, \nu_y) = F_{\lambda,z_0} \cdot U_0(\nu_x, \nu_y).$$

By composition with the Fourier operator $\mathcal{F}$ and its inverse, the propagation operator in real space domain $P_{\lambda,z}$ can be constructed as

$$u_{z_0}(x, y) = P_{\lambda,z_0} \cdot u_0(x, y) = \mathcal{F}^{-1} \cdot F_{\lambda,z_0} \cdot \mathcal{F} \cdot u_0(x, y),$$

so that

$$P_{\lambda,z} = \mathcal{F}^{-1} \cdot F_{\lambda,z} \cdot \mathcal{F}. \tag{2.10}$$

2.1.5 Evanescent waves

So far, we restricted our analysis to wavefronts for which the spatial spectrum had a limited bandwidth so that

$$|\boldsymbol{\nu}| > \nu_0 \implies U(\boldsymbol{\nu}) \ll 1.$$

However, a general wavefront could contain high spatial frequencies for example due to interaction with a hard aperture, and the plane wave model does not cover such cases.

If we simply substitute a wave with the form of a complex plane wave and force $k_x^2 + k_y^2 > k_0^2$, then from equation 2.7 it must be that k_z is purely imaginary. As in the case where k_z is real, the square root operation leaves the sign undetermined. Mathematically, both solutions are valid, but physically they lead to two very different situations. One of the solutions grows exponentially as z increases, while the other one decays exponentially. The sign of k_z depends on the sign that we assign to the spatial dependence of the complex exponential[6], in this case negative. Therefore, the sign of the imaginary k_z needs to be negative to give a decaying exponential, and equation 2.8 needs to be revised to become

$$k_z = \left(\sqrt{k_0^2 - k_x^2 - k_y^2}\right)^*. \tag{2.11}$$

Note how the complex conjugation does not change the behavior when the solution is real.

This exponentially decaying solutions are known as evanescent waves, and are a phenomenon that occurs when a disturbance has a wavevector in any direction which is larger than the wavevector of a plane wave at the same frequency. It can occur as mentioned when a hard aperture is present, which introduces high spatial frequency components, or when the wave transitions to another medium where the wavelength at the wave's frequency becomes larger, as it is the case for total internal reflection.

[6]Which in turn depends on the (arbitary) sign in the exponent of the time dependence phasor.

2.1.6 Effects of thin optical elements on wavefronts

A thin optical element acts locally on the wavefront by changing the amplitude or phase. A linear and time invariant thin optical element can be simply represented as a position dependent multiplicative factor that transforms wavefronts traveling through it.

A simple example can be an opaque thin film with a circular aperture of radius r_0, centered at the origin. The spatial transfer function of such an element is of the form

$$a(x,y) = \begin{cases} 1 & \text{if } \sqrt{x^2+y^2} < r_0 \\ 0 & \text{otherwise,} \end{cases}$$

which given an incident wavefront $u(x,y)$ produces the new wavefront $v(x,y)$ after the aperture:

$$v(x,y) = a(x,y) \cdot u(x,y).$$

2.1.7 Paraxial approximation

A wavefront is said to be paraxial when it has most of its energy in spectral components which propagate at a small angle with respect to the z-axis, which is equivalent to the condition that there exists a $\nu_1 \ll \nu_0$ such that

$$|\boldsymbol{\nu}| > \nu_1 \implies U(\boldsymbol{\nu}) \ll 1.$$

When dealing with paraxial optical fields, the propagation phase in 2.9 can be approximated by the first term in its series expansion[7]:

$$k_0 z_0 \sqrt{1-(\lambda_0\nu_x)^2-(\lambda_0\nu_x)^2} \approx k_0 z_0 \left[1 - \frac{1}{2}(\lambda_0\nu_x)^2 - \frac{1}{2}(\lambda_0\nu_y)^2\right].$$

The propagation of the Fourier components then can be rewritten as

$$U_{z_0}(\nu_x,\nu_y) = \exp(-jk_0z_0) \cdot \exp\left\{jk_0z_0\frac{1}{2}\left[(\lambda_0\nu_x)^2+(\lambda_0\nu_y)^2\right]\right\} U_0(\nu_x,\nu_y), \qquad (2.12)$$

[7]In the paraxial approximation k_z is never imaginary, so we can ignore the complex conjugation.

from which it is clear that in the paraxial limit propagation consists of a phase shift equivalent to that of a plane wave, plus an additional quadratic phase correction.

Since by assumption the quantity $1/2\left[(\lambda_0\nu_x)^2 + (\lambda_0\nu_y)^2\right]$ is small, then over a short distance the quadratic correction is negligible, and propagation can be approximated simply by a constant phase shift for all the spatial frequencies, which in turn means also a constant phase shift in the real wavefront.

In the paraxial approximation, it is possible to recover the electric field from the scalar wave, assuming that the polarization $\hat{\boldsymbol{n}}$ of the vector potential is perpendicular to the z-axis. If it is the case,

$$\boldsymbol{E} = -j\omega\left(\boldsymbol{A} + \frac{1}{\omega^2\mu_0\epsilon}\nabla\nabla\cdot\boldsymbol{A}\right). \tag{2.13}$$

The time averaged Poynting vector, which can be interpreted as the local power flux density in an electromagnetic wave, can be found from the complex fields as

$$|\langle\boldsymbol{S}\rangle| = \frac{1}{2}|\mathrm{Re}(\boldsymbol{E}\times\boldsymbol{H}^*)| = \frac{1}{2}\frac{|\boldsymbol{E}|^2}{Z}$$

where Z is the impedance of the medium.

Using equation 2.13, and neglecting the second term, the intensity in the $\hat{\boldsymbol{z}}$ direction can be expressed in terms of the scalar wavefront as

$$I(x,y) = \frac{1}{2Z_0}n\omega_0^2|u(x,y)|^2, \tag{2.14}$$

where Z_0 is the impedance of vacuum (about 377 Ω) and $n = \sqrt{\epsilon/\epsilon_0}$ is the refractive index of the medium.

2.2 Two mirror resonators

A two mirror resonator is composed of two mirrors facing each other, allowing for a standing optical wave to exist in the space between them. If the mirrors are perfect reflectors separated by a distance L, the allowed frequencies for the standing waves

are those of the wave with $\lambda = 2L$ and of its harmonics. The spacing between the allowed frequencies of resonance is called the free spectral range (FSR) of the cavity and it is given by $\Delta\nu = c/2L$. A cavity mode needs to be resonating longitudinally, or in other words its frequency needs to be a multiple of the FSR.

Furthermore, a real cavity necessarily has finite extent, so the mirrors need to be focusing and the transverse resonances occur when the spreading due to diffraction is canceled by the focusing. In this section I will review briefly the properties of the modes of two spherical-mirror cavities in the paraxial limit.

2.2.1 Longitudinal resonance

Since energy has to be transferred into the cavity to the modes, at least one of the mirrors needs to be partially transmissive to let the light in. It is possible to understand the resonant behavior and the nature of intensity enhancement in such a cavity by following the path of an optical wave through multiple passes, as in figure 2-2. Such a setup is also used as an interferometer due to the possibility of obtaining very narrow band resonances, and it is known as a Fabry-Perot interferometer.

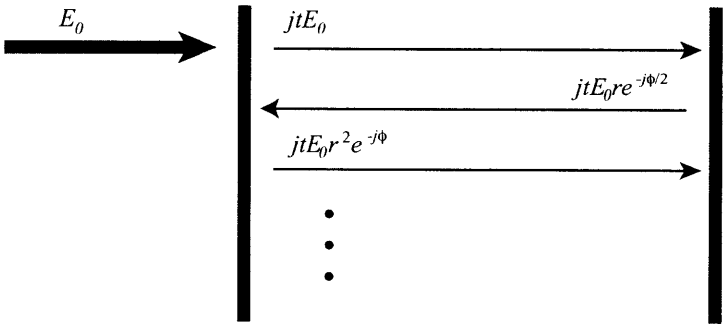

Figure 2-2: Multipass interference inside a Fabry-Perot resonator.

Suppose that both mirrors reflect a fraction R of the incident power, and that the phase shift is π upon reflection and $\pi/2$ upon transmission[8]. The field reflection and

[8]Appropriate reference planes before and after the mirror can be chosen so that the phase shift is exactly as assumed.

transmission coefficients can be found from the power reflectance to be $r = \sqrt{R}$ and $t = \sqrt{1-R}$ respectively.

Referring to the figure, during the first pass the transmission from the incoming plane wave of amplitude E_0 will be jtE_0. The wave will then propagate across the cavity, acquiring a phase $\phi/2 = \omega L/c$ before being reflected backwards, retaining only a fraction r if the field. Again, the wave will propagate across the cavity and be reflected, so that its amplitude has been changed by a factor of $r^2e^{-j\phi}$. If all the successive passes are interfered with each other, the final complex amplitude inside the cavity will be

$$E_{fp} = jtE_0 \cdot (1 + r^2e^{-j\phi} + (r^2e^{-j\phi})^2 + \ldots) = \frac{jt}{1 - r^2e^{j\phi}}E_0. \tag{2.15}$$

If $\phi = 0$, and assuming $1 - R \ll 1$,

$$|E_{fp}| \approx \frac{1}{t}|E_0|, \tag{2.16}$$

which in turns means that the intensity is enhanced approximately by a factor of $(1-R)^{-1}$.

The intensity of the resonant wave can be shown from equation 2.15 to have the following dependence on phase:

$$|E_{fp}|^2 \approx \frac{1-R}{(1-R)^2 + 4R\sin^2(\phi/2)}|E_0|^2,$$

which when plotted as a function of ω shows a series of equally spaced resonances.

2.2.2 Transverse resonance

In a real cavity with spherical mirrors, there will be a set of wavefronts that are in resonance around a given ω, meaning that propagation through the cavity and the focusing effect of the mirrors cancel out, and the wavefront profile is unaltered after a roundtrip.

For the design of this cavity, it suffices to know that in the paraxial approximation

it is possible to derive[9] a set of modes that are separable in rectangular coordinates, and whose transverse profile is that of a gaussian modulated by Hermite polynomials for each of the axes. A mode can then be characterized by three quantum numbers m, n, q, which identify the mode order along the x-, y- and z-axis respectively; the mode will resonate at the frequency

$$f_{mnq} = \frac{c}{2L}\left[q + \frac{m+n+1}{\pi}\cos^{-1}\left(1 - \frac{L}{R_0}\right)\right], \tag{2.17}$$

given the radius of curvature of the mirrors R_0 (from [13]).

Another complete set of modes can be constructed by separating the variables in polar coordinates, the Laguerre-Gaussian modes, which are gaussians modulated radially by a Laguerre polynomial, and azimuthally by circular harmonics. Since both sets of modes are complete sets, the basis elements of one can be rewritten in terms of the elements of the other, as done in [14].

Some of the Laguerre-Gaussian modes transverse intensity patterns can be seen in figure 5-2.

2.3 Phase of the atomic polarization during HHG

For any process where harmonics are generated, it is very important that the harmonic wave's phase stays fixed with respect to the fundamental wave's phase[10]. If the phase relationship changes as the waves propagate, at a certain point the newly generated harmonic field will be out of phase with the field generated previously, and destructive interference will greatly reduce the harmonic output.

By knowing the amount of phase mismatch, it is possible to limit the extent of the region where the harmonics are generated so that by the time the waves would interfere destructively there is no more harmonic generation. In the case of HHG, phase mismatch can be very severe because the harmonics involved are usually very

[9]The interest reader should look at [12] for a detailed derivation and analysis of the modes of a two mirror cavity.

[10]Once the trivial phase dependence from plane wave propagation is factored out.

high and the phase mismatch for the process exceeds the phase mismatch of the fundamental field by a factor of the harmonic order.

The two prevailing phase effects to be taken into account for HHG are the Guoy phase shift of the driving beam and the phase of the appropriate frequency component of the atomic polarization in response to the driving beam, which is effectively the phase of the harmonic field. The former is a geometric property of the beam, while the latter depends locally on the intensity, the frequency of the fundamental, and the order of the harmonic of interest. Detailed theoretical calculations in [1] have shown that the dipole phase can be approximated very well by a piecewise linear function, shown in figure 2-3.

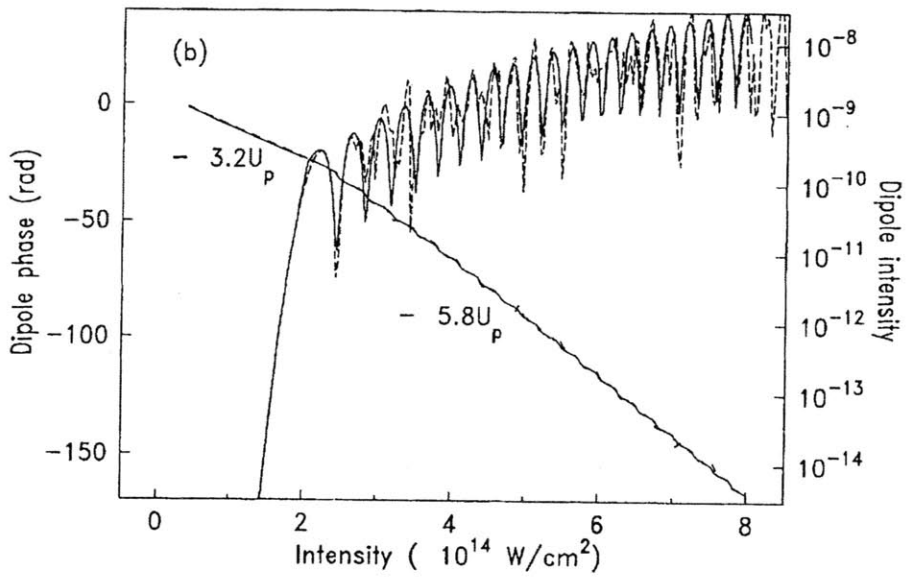

Figure 2-3: Phase of the atomic polarization for a single neon atom at the 45th harmonic of a 825 nm driving field, from [1].

The independent variable is the ponderomotive energy U_p, the average kinetic energy of an electron in an oscillating field, given by

$$U_p = \frac{e^2|\boldsymbol{E}|^2}{4m_e\omega^2}$$

for a linearly polarized plane wave of amplitude $|\boldsymbol{E}|$ at a frequency ω, where e and m_e are the charge and mass of the electron, respectively. For a given laser frequency,

U_p is then proportional to the intensity.

The ponderomotive energy is a property of the laser field, and it is crucial in various aspects of HHG. The highest harmonic generated in the plateau has a photon energy equal to approximately $3.17U_p$. Harmonics with higher energies are located in the cutoff region, where there is no significant harmonic generation.

The cutoff frequency then is determined by the intensity of the laser (given ω). The photon energy of the nth harmonic is simply $n\hbar\omega$, and it determines the point where the change of slope occurs: if the harmonic is above cutoff (i.e. $3.17U_p < n\hbar\omega$) then the slope is approximately $-3.2U_p$ in atomic units normalized so that $\omega = 1$, whereas if the harmonic is in the plateau region the slope becomes $-5.8U_p$. Conversion to atomic units is detailed in section 4.5.

Chapter 3

Mathematical theory behind the numerical simulator

I adapted the techniques of wave optics to be suitable for computer implementation and to be integrated with scattering matrices to provide a description of optical systems composed of many linear dielectric sections and thin optical elements, and to simulate and analyze such systems. The most important analysis of a resonator for this study is that of its eigenmodes, which constrains the resolution of the wavefront due to the computational space and time requirements. Since the systems of interest to this study exhibit circular symmetry[1], the wavefronts are assumed to be separable in polar coordinates:

$$u(x = r\cos\theta, y = r\sin\theta) = u_r(r) \cdot u_\theta(\theta),$$

and the transfer functions of all the optical elements are assumed to have circular symmetry and so have the form $a(x, y) = a_r(\sqrt{x^2 + y^2})$.

Since calculations are done on the computer, wave propagation can be calculated from the exact propagation operator (equation 2.10), without assuming the paraxial condition. The simulation is still limited to paraxial systems however, because thin optical elements are used in place of the real transfer functions for the elements, and

[1] As well as most systems in optics, where astigmatism effects can be neglected.

in any case the scalar wave approximation ceases to hold true when the angle between the electric field and the vector potential is large.

3.1 Finite discrete description of wavefronts and linear optical elements

The wavefronts described in the previous chapter are complex functions with the entire $\mathbb{R}^2$ as the domain. To perform numerical calculations, the wavefronts need to be sampled at a discrete and finite number of points (denoted by N), thus the wavefronts become complex vectors[2]. Each component of the wavefront vector represents the value of the continuous wavefront at a particular point of the continuous domain. Likewise, each component of the spatial frequency vector represents the complex value of the spectrum at a particular point in the continuous spatial frequency domain. Let us denote the wavefront vector as $\boldsymbol{u}$ and the spatial frequency vector as $\boldsymbol{\nu}$.

Since the Fourier transform[3] is a linear operator, it is reasonable to assume that it is possible to create a discrete and finite linear operator that implements the Fourier transform between the two discrete domains. Such an operator is simply a square complex matrix which is invertible and in the ideal case numerically stable such that

$$\boldsymbol{\nu} = \mathcal{F}\boldsymbol{u}$$

and

$$\boldsymbol{u} = \mathcal{F}^{-1}\boldsymbol{\nu}.$$

Finding the appropriate sets of points of discretization for which there exists a discrete transform able to represent correctly the continuous transform[4] on the

[2]There are also effects due to quantization, since a 64-bit double precision floating point number cannot represent a real number. However, this aspect can be ignored since the dynamic range is very high (18 decimal digits) so that the fractional error in the calculations is still unnoticeable even with a large number of points.

[3]For brevity I will loosely refer to any transform to the frequency domain as *Fourier transform*, unless more specificity is needed.

[4]By which we mean that the inverse of the discrete transform matrix also represents the contin-

discrete domain is not trivial in general, and it is not of interest for this work. It suffices to know that exact discrete and finite matrix representations exist for the DFT (discrete Fourier transform), as well as for the qDHT (quasi-discrete Hankel transform, discussed in section 3.2).

Once a matrix expression for the Fourier transform is obtained, by knowing the points of discretization in the frequency domain it is possible to create the matrix for the operator $F_{\lambda,z}$. Since the operator is in the frequency domain, the matrix is diagonal:

$$F_{i,i} = exp\left(-jkz\sqrt{1-(\lambda\nu_i)^2}^*\right),$$

where ν_i is the spatial frequency of the ith discretization point, and corresponding to the ith component of $\boldsymbol{\nu}$.

With the matrices for the Fourier transform and its inverse and the matrix for wave propagation in frequency domain, the propagation matrix in the spatial domain can be easily obtained, since

$$P_{\lambda,z} = \mathcal{F}^{-1} \cdot F_{\lambda,z} \cdot \mathcal{F}. \tag{3.1}$$

Equation 3.1 is identical to equation 2.10, but the important difference is that here the operators are $N \times N$ complex matrices, as opposed to linear operators acting on functions $\mathbb{R}^2 \to \mathbb{C}$.

Thin optical elements are trivial to convert to matrix form in the spatial domain. They are represented by a diagonal matrix whose entries have the same value as the element transfer function at the corresponding point of discretization.

The representation of wave propagation and of optical elements as matrices provides us with a simple way of calculating the eigenmodes of a resonator. Consider for example a symmetric linear cavity made with two identical spherical mirrors separated by a distance L, as shown in figure 3-1. Let us imagine that we can follow a generic wavefront $u(\boldsymbol{r})$ that is propagating in the cavity, starting at the center. First of all, it will propagate for a distance $L/2$, then the mirror will add a quadratic

uous inverse transform in the reduced domain.

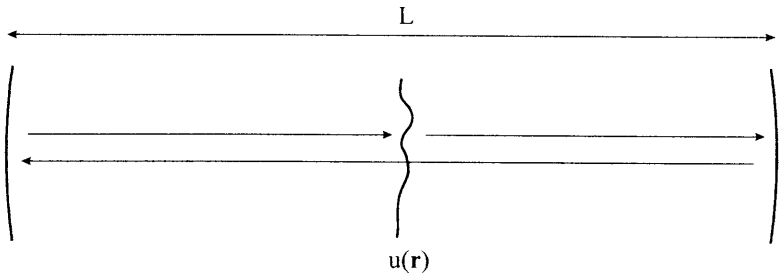

Figure 3-1: A resonant wavefront undergoes a roundtrip of the cavity without altering its spatial pattern, up to a multiplicative constant.

phase, and finally the wavefront will propagate $L/2$ more to be again at the center of the cavity, this time going in the opposite direction. If we follow again the same path, going in the other direction, the wavefront will now be in the same point as the beginning, going in the same direction.

What distinguishes the wavefront of a resonant mode of the cavity from any other wavefront is that after one roundtrip it has changed only by a multiplicative factor. In other words, its finite representation is an eigenvector of the matrix T, describing the transformation that occurs in a roundtrip in the cavity. In this case, if we call M the matrix representation of the mirrors,

$$T = (F_{\lambda,L/2} \cdot M \cdot F_{\lambda,L/2})^2. \tag{3.2}$$

An eigenmode $\boldsymbol{u}_m$ of the cavity will solve the eigenvalue equation

$$\lambda \boldsymbol{u}_m = T \cdot \boldsymbol{u}_m$$

for some complex number λ, which represents the attenuation and phase shift[5] over the course of a roundtrip. The total energy after one roundtrip is a fraction $|\lambda|^2$ of the initial energy.

A more complete formalism to find the resonances of cavities with elements inside

[5]The context should make clear when λ is an eigenvalue as opposed to the wavelength.

of them is presented in section 3.4, but the underlying idea is the same as for the simple algorithm presented here. This simple algorithm ignores the longitudinal condition for resonance, however the eigen-wavefronts' transverse shapes are still correct in the paraxial approximation, as shown in [15].

3.2 The quasi-discrete Hankel transform

Since for N discretization points the size of the matrices needed to describe the Fourier transform and the optical elements is $N \times N$, it is very useful to take advantage of symmetries to reduce the number of points. Since the systems of interest present circular symmetry (i.e. all the optical elements have transfer functions whose value depends only on the distance from the central axis), all the modes of the systems will be separable when parameterized in terms of r, the distance from the axis of symmetry, and θ, the angular position around the axis[6].

If the sampling points are approximately equally spaced, a transform that uses N radial points has the same resolution of a $2N \times 2N$ rectangular grid, but requiring a matrix of only N^2 elements as opposed to $16N^4$, giving us the possibility of studying fairly large systems at sub wavelength resolution.

Before going any further, it is important to note here that in the case where only wave propagation is involved there is an advantage in using rectangular grids, for in that case there is no need of explicitly creating the transform matrices since the 2D FFT can be used instead. The time complexity of computing wave propagation becomes in that case $O(N^2 log N)$, whereas for a transform taking advantage of symmetry but using an explicit representation it will take time $O(N^2)$ to compute[7]. The extra flexibility in terms of input wavefronts comes at the price of a small hit in performance.

[6]Or if the modes are degenerate, they can always be combined appropriately in another complete set of modes that is separable in that way.

[7]There are indeed algorithms for computing fast Hankel transforms, but their numerical accuracy is not the same as that of the "slow" version used in this study. Achieving the same numerical accuracy would require to increase N to the point where the time complexity is similar. Conversely, the FFT retains the same accuracy as the discrete Fourier transform, so it should be used by all means when possible.

However, in situations where it is necessary to calculate the eigenmodes of a resonator, or to simulate a system with multiple reflections, an explicit matrix representation is required.

In the continuous case, the Fourier transform of a function separable in polar coordinates can be written as a weighted sum of Hankel transforms (from [11]):

$$\mathcal{F}\{g(r,\theta) = g_r(r)g_\theta(\theta)\} = \sum_{p=-\infty}^{\infty} c_p(-j)^p \exp(jp\phi)\mathcal{H}_p\{g_r(r)\},$$

where the expansion coefficients are given by

$$c_p = \frac{1}{2\pi}\int_0^{2\pi} g_\theta(\theta)\exp(-jp\theta)\,\mathrm{d}\theta,$$

and the Hankel transform of integer order p is given by

$$\mathcal{H}_p\{g_r(r)\} = 2\pi\int_0^{\infty} r g_r(r) J_p(2\pi r\nu)\,\mathrm{d}r,$$

where ν and ϕ are the radial and azimuthal coordinates in spatial frequency domain.

If the angular dependence of the wavefront is of the form $\exp(jp\theta)$ for some integer p, then the expansion coefficients will all be zero except for $c_p = 1$. In that case, the Hankel transform provides a way of calculating the radial dependence in Fourier domain given the wavefront, while its inverse

$$\mathcal{H}_p^{-1}\{G_r(\nu)\} = 2\pi\int_0^{\infty} \nu G_r(\nu) J_p(2\pi\nu r)\,\mathrm{d}\nu$$

performs the reverse calculation.

The quasi-discrete Hankel transform (qDHT) is the discretized and finite version of the continuous Hankel transform, and it has the desirable property that the inverse of its matrix representation is the discretized and finite version of the continuous inverse Hankel transform.

The transform can be expressed in terms of n and m, the indices for the space and spatial frequency discretization points, which are also the indices of the discretized

vectors coordinates, as

$$F\left(\nu = \frac{\alpha_{pm}}{2\pi R}\right) = \frac{1}{\pi V^2} \sum_{n=1}^{N} \frac{f(r = \alpha_{pn}/2\pi V)}{J_{p+1}^2(\alpha_{pn})} J_p\left(\frac{\alpha_{pn}\alpha_{pm}}{S}\right), \tag{3.3}$$

$$F\left(r = \frac{\alpha_{pn}}{2\pi V}\right) = \frac{1}{\pi R^2} \sum_{m=1}^{N} \frac{F(\nu = \alpha_{pm}/2\pi R)}{J_{p+1}^2(\alpha_{pm})} J_p\left(\frac{\alpha_{pn}\alpha_{pm}}{S}\right), \tag{3.4}$$

where α_{pi} is the ith zero of the Bessel function J_p, and p is the order of the transform. R is the limit radius for the simulation, while V is the limit bandwidth. The space-bandwidth product is given by

$$S = 2\pi RV = \alpha_{p,N+1}$$

and it is constant given the number of points and the transform order.

While the formulas look intimidating, they are simply dot products of the vectors $\boldsymbol{r}$ or $\boldsymbol{\nu}$ with constant vectors that depend only on the parameters of the transform, therefore the transform and its inverse are simply a matrix multiplication.

The quasi-discrete Hankel transform was introduced in [16]. My implementation follows the work of [17], where the transform matrix and its inverse are created from a unitary matrix $\boldsymbol{T}$ which depends only on p and N, and which is changed appropriately to the transform and inverse matrix depending on the value of R.

3.3 Simulation of thin optical elements

Thin optical elements are simply space-dependent multiplicative factors for the simulated wavefront. By appropriately choosing the magnitude and phase of the filter, all the common linear optical elements can be simulated in the paraxial approximation. Even though circular symmetry is assumed, the filters derived in this section can trivially be converted to rectangular coordinates.

3.3.1 Hard apertures, partially transmitting elements and phase masks

The simplest element to simulate is probably a circular hard aperture, shown in figure 3-2. This system acts like a filter, blocking out the portions of the wavefront that are farther from the central axis than a fixed radius r_0. Given the discretization points r_i, its matrix representation is diagonal, and given by

$$A_{ii} = \begin{cases} 1 & \text{if } r_i < r_0 \\ 0 & \text{otherwise.} \end{cases}$$

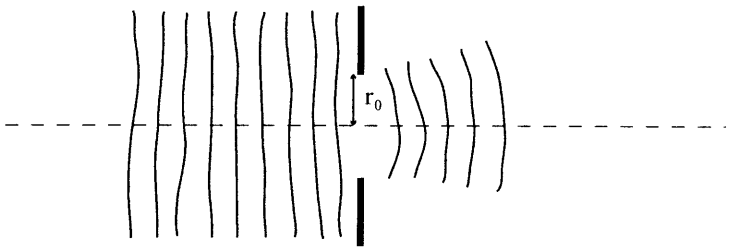

Figure 3-2: Effect of a hard aperture on wavefronts.

Obviously we are not limited to all-or-none filters. For example, a filter for which the transmitted intensity goes down linearly as the radius increases, with full transmittance at the center and complete cutoff for $r > r_0$ can be described by the matrix

$$A_{ii} = \begin{cases} \sqrt{1 - r_i/r_0} & \text{if } r_i < r_0 \\ 0 & \text{otherwise,} \end{cases}$$

where the square root is needed because the matrix multiplies the wavefront complex amplitude, whereas intensity is given by the magnitude squared.

In a similar way it is possible to construct matrices for phase-only elements, or elements with both phase and magnitude transfer functions. It is possible to introduce gain if the magnitude of the matrix elements is greater than 1.

3.3.2 Thin lenses

Lenses can be represented as a phase only element, without losses. In the case of thin lenses, the only parameter that characterizes them is the focal length f, which can be found from the material's index of refraction and the radii of curvature of the two surfaces[8]:

$$\frac{1}{f} \approx (n-1)\left(\frac{1}{R_1} - \frac{1}{R_2}\right).$$

We can use $R_2 = \infty$ to easily calculate the phase shift at different radii, as shown in figure 3-3. The overall phase can be ignored, so we set arbitrarily $\phi(r = 0) = 0$ and compute the additional phase shift that the parts of the wavefront experience at different r.

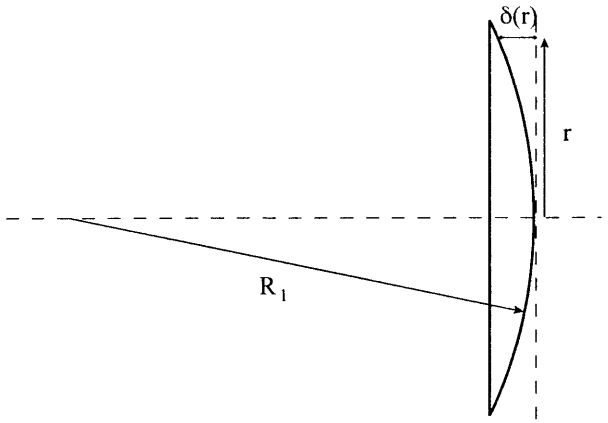

Figure 3-3: Calculation of the matrix representation of a thin lens.

To evaluate $\delta(r)$, the path that the wavefront travels in air before reaching the lens' surface, assume that the lens is at $z = 0$. Then its surface can be described by

$$z(r) = R_1 - \sqrt{R_1^2 - r^2} = R\left(1 - \sqrt{1 - \left(\frac{r}{R_1}\right)^2}\right) \approx \frac{1}{2R}r^2,$$

where the quadratic approximation is valid if the lens is thin. Since $\delta(r) = z(r)$, the extra optical path undergone by light inside the lens at the center with respect to the light at distance r is $(n-1)\delta(r)$. The light propagating in the center will acquire

[8]Assuming that the lens is in a medium with $n = 1$.

more phase at a given z, since the optical pathlength is longer there, so since phase goes negative as propagation occurs, a positive phase factor needs to be added:

$$L_{ii} = \exp(jk_0(n-1)\delta(r)) = \exp\left(jk_0(n-1)\frac{1}{R_1}\frac{r^2}{2}\right) = \exp\left(jk_0\frac{r^2}{2f}\right).$$

This formula is valid for concave lenses too, by using $f < 0$, and it applies to wavefronts coming from both sides of the lens. The reflection due to index mismatch is ignored, as well as the possible multiple internal reflections. The reason for not pursuing a more detailed model is that, even without AR coatings, lenses are elements in a system through which the wavefront usually passes only once, as opposed to the mirrors in a resonator for example.

Note how the paraxial approximation is crucial in the derivation of this matrix representation, since in general it is not true that propagation for a short distance can simply be treated as a phase shift.

3.3.3 Mirrors

Mirrors are the fundamental element in optical resonators. Unlike the case of lenses, the light in a system often is reflected multiple times by the same mirror, and it becomes important to take into account both the reflected and transmitted beam.

In the case of a flat mirror with no losses, there is going to be a certain relationship between the phase of the incoming wavefront and that of the reflected and transmitted wavefronts. Conventionally, the phase of the reflectivity and transmissivity is chosen so that given the incident wavefront $u_i(\boldsymbol{r})$

$$u_r(\boldsymbol{r}) = -ru_i(\boldsymbol{r})$$

$$u_t(\boldsymbol{r}) = jtu_i(\boldsymbol{r}),$$

where u_r and u_i are the reflected and transmitted wavefronts, and for a lossless mirror which reflects a fraction R of the incoming power the amplitude reflection and

transmission coefficients are

$$r = \sqrt{R},$$

$$t = \sqrt{1-R} = \sqrt{1-r^2}.$$

A flat mirror will have the same operator form for wavefronts coming from either direction. Mirrors used in resonators though are usually concave, as shown in figure 3-4. The reflecting surface is deposited onto a concave substrate with refractive index n and curvature R_0, therefore the effect on the incoming wavefronts varies depending on which side of the mirror is encountered first.

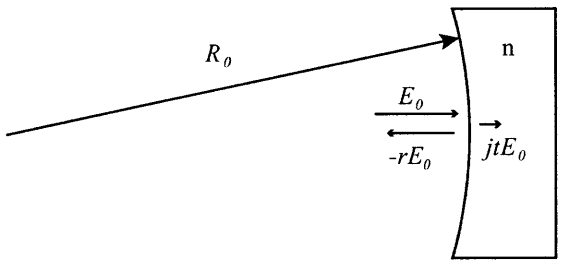

Figure 3-4: Calculation of the matrix representation of a mirror.

If the reflecting surface is encountered first, the reflected wavefront will acquire a phase equivalent to that of a lens[9] with $f = R_0/2$, while the transmitted one will be refracted by the substrate, a plano-concave lens with

$$f = -\frac{R_0}{n-1}.$$

Therefore, for wavefronts incident to the reflecting surface first,

$$u_r(r_k) = -r \exp\left(jk_0 \frac{r_k^2}{R_0}\right) u_i(r_k),$$

$$u_t(r_k) = jt \exp\left(-jk_0 \frac{r_k^2(n-1)}{2R_0}\right) u_i(r_k).$$

[9]Because the phase mismatch between parts of the wave at different radius is quadratic: $2k \cdot r^2/2R_0$.

For the wavefronts which are incident on the substrate first, the transmitted component will pass through the substrate, so it will undergo the same phase shift and the expression is unchanged. The reflected component, on the other hand, will traverse the substrate twice, so its relation to the incident wavefront is

$$u_r(r_k) = -r \exp\left(-jk_0 \frac{nr_k^2}{R_0}\right) u_i(r_k).$$

3.4 Linear optical systems

Using the methods described above to calculate the effects on the wavefronts of propagation and interaction with thin elements, it is possible to develop a convenient and scalable representation of linear optical systems that are constrained between two parallel planes.

3.4.1 Scattering matrices

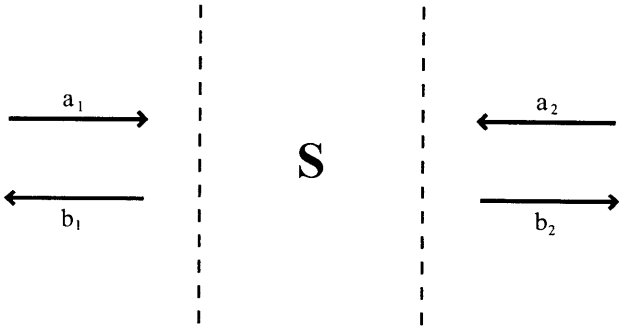

Figure 3-5: Wavefronts naming conventions with scattering matrices.

Any linear system of this form can be entirely characterized by a scattering matrix, relating the two wavefronts propagating out of the reference planes b_1 and b_2 to the two incoming ones a_1 and a_2, as shown in figure 3-5. S is a 2×2 matrix whose elements

are linear operators on wavefronts[10], and will be denoted as

$$\mathbf{S} = \begin{pmatrix} S_{11} & S_{12} \\ S_{21} & S_{22} \end{pmatrix}.$$

If the inputs to the system (i.e. a_1 and a_2) are known, the outputs can be found by applying the scattering matrix:

$$b = \mathbf{S}a,$$

or written by components

$$b_1 = S_{11}a_1 + S_{12}a_2$$

$$b_2 = S_{21}a_1 + S_{22}a_2.$$

Scattering matrices for both propagation in a dielectric and interaction with a thin element can be easily constructed. In the first case, the incoming wavefronts propagate through the material and leave on the other side, without any back reflection. For a propagation distance d in a medium with refractive index n, the scattering matrix for wavefronts with wavelength λ_0 in vacuum will then simply be

$$\mathbf{S} = \begin{pmatrix} 0 & F_{\lambda_0/n,d} \\ F_{\lambda_0/n,d} & 0 \end{pmatrix}.$$

In the case of a thin element, the operators S_{ij} can be defined in terms of the filtering transfer functions $s_{ij}(x,y) : \mathbb{R}^2 \to \mathbb{C}$ so that $S_{ij}u(x,y) = s_{ij}(x,y) \cdot u(x,y)$. There are four separate filtering functions: two for transmission and two for reflection (one in each direction). For example, a thin film that absorbs half of the power of

[10]In the discrete and finite case, $\boldsymbol{S}$ is a 2×2 matrix of $N \times N$ complex matrices, or a $2N \times 2N$ complex matrix. However, the formalism derived in this section is completely generic, so it is described in the notation of continuous wavefronts and of the linear operators acting on them.

the light going through it can be represented simply as

$$\mathbf{S} = \begin{pmatrix} 0 & \frac{1}{\sqrt{2}} \\ \frac{1}{\sqrt{2}} & 0 \end{pmatrix},$$

while a mirror reflecting about 98% of the light coming from both sides and absorbing the rest, as might be the case for a layer of silver for some wavelengths, can be represented as

$$\mathbf{S} = \begin{pmatrix} 0.99 & 0 \\ 0 & 0.99 \end{pmatrix}.$$

Similarly, the scattering matrices for the elements analyzed in section 3.3 can be constructed by evaluating the appropriate spatially dependent multiplicative factor at the points of discretization.

Deriving scattering matrices for more complex systems becomes a difficult task, so it is convenient to be able to compute the scattering matrix of a composite system made of a succession of simple systems for which the scattering matrices can be constructed easily.

3.4.2 Transfer matrix composition technique

A technique of microwave electronics commonly used in optics is to convert the scattering matrices of the elements of the system into transfer matrices. The transfer matrix is a 2×2 matrix of operators whose elements satisfy the following relation in terms of the wavefronts of figure 3-5:

$$\begin{pmatrix} b_2 \\ a_2 \end{pmatrix} = \begin{pmatrix} T_{11} & T_{12} \\ T_{21} & T_{22} \end{pmatrix} \cdot \begin{pmatrix} a_1 \\ b_1 \end{pmatrix}.$$

The important difference with the S-matrix is that a T-matrix relates inputs and outputs on one side of the system to inputs and outputs to the other side. Now, if we arbitrarily take the wavefronts on the left side of the system as the known quantity, we can recover the wavefronts on the right side. If we cascade another system, the

wavefronts to the right of the first system become the wavefronts to the left of the second one, and can be transformed again with the T matrix of the second system.

Therefore, the T-matrix of a composed system is simply the composition of the T-matrices of the constituents:

$$\mathbf{T} = \mathbf{T}_n \cdot \mathbf{T}_{n-1} \cdot \cdots \cdot \mathbf{T}_2 \cdot \mathbf{T}_1,$$

or for just two systems, $\mathbf{T}_2 \circ \mathbf{T}_1 = \mathbf{T}_2 \cdot \mathbf{T}_1$, where $\circ$ represents composition of systems, while $\cdot$ represents matrix multiplication.

Using the transfer matrices we have a simple way of cascading systems, but this method has two severe drawbacks. First, the transfer matrix will be unstable when the underlying scattering matrix contains wave propagation, since determining a_2 from b_1 will involve inverse propagation, with the exponential explosion of any evanescent component[11].

An even more serious problem is that transfer matrices require that the optical system is invertible, so that one of its inputs can be recovered from the other input and one of the outputs. This operation is impossible even for a simple system such as an aperture. The portion of the a_2 wavefront that is filtered out will never reach b_1, so it is impossible to recover that lost information and recreate a_2. Since there is no solution to this problem, a different approach is needed.

3.4.3 Direct composition of S-matrices

The technique that I developed to be able to calculate the input-output relationships of cascaded systems, while at the same time being able to reconstruct what happens at the interface between the constituents, allows to overcome the limitations of the transfer matrix technique.

The generic system shown in figure 3-6 is composed by cascading two systems with known S-matrices, $\mathbf{S}'$ and $\mathbf{S}''$. To solve for b_1 and b_2, we need to calculate a and

[11] Very small evanescent components will always be present due to numerical artifacts. The only way around this problem is to completely ignore evanescent waves.

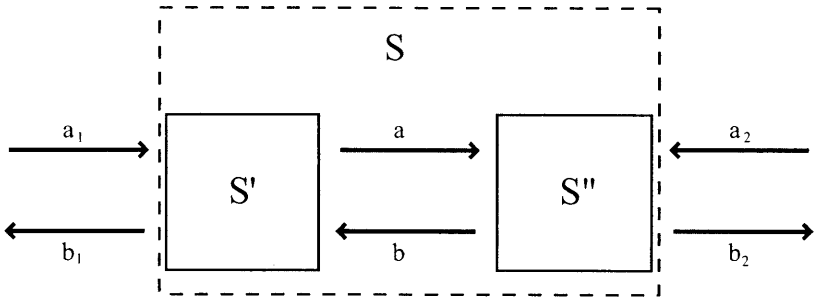

Figure 3-6: Wavefront naming convention for composition of S-matrices.

b in terms of a_1 and a_2.

The scattering relations of the two subsystems are

$$\begin{pmatrix} b_1 \\ a \end{pmatrix} = \begin{pmatrix} S'_{11} & S'_{12} \\ S'_{21} & S'_{22} \end{pmatrix} \cdot \begin{pmatrix} a_1 \\ b \end{pmatrix} \qquad \begin{pmatrix} b \\ b_2 \end{pmatrix} = \begin{pmatrix} S''_{11} & S''_{12} \\ S''_{21} & S''_{22} \end{pmatrix} \cdot \begin{pmatrix} a \\ a_2 \end{pmatrix}$$

which give the following relations:

$$a = S'_{21}a_1 + S'_{22}b \qquad b = S''_{11}a + S''_{12}a_2$$

Substituting the second one into the first one gives

$$\begin{aligned} a &= S'_{21}a_1 + S'_{22}S''_{11}a + S'_{22}S''_{12}a_2 \\ (\mathbb{I} - S'_{22}S''_{11})a &= S'_{21}a_1 + S'_{22}S''_{12}a_2 \\ a &= (\mathbb{I} - S'_{22}S''_{11})^{-1} \cdot (S'_{21}a_1 + S'_{22}S''_{12}a_2), \end{aligned}$$

and the reverse gives

$$b = (\mathbb{I} - S''_{11}S'_{22})^{-1} \cdot (S''_{11}S'_{21}a_1 + S''_{12}a_2),$$

so the wavefronts at the interface of the two systems are known. The two outgoing wavefronts of the composite system can then be found directly using the scattering

matrices of the component systems:

$$b_1 = S'_{11}a_1 + S'_{12}b = S'_{11}a_1 + S'_{12}(\mathbb{I} - S''_{11}S'_{22})^{-1} \cdot (S''_{11}S'_{21}a_1 + S''_{12}a_2),$$

$$b_2 = S''_{21}a + S''_{22}a_2 = S''_{21}(\mathbb{I} - S'_{22}S''_{11})^{-1} \cdot (S'_{21}a_1 + S'_{22}S''_{12}a_2) + S''_{22}a_2$$

The rule for composing scattering matrices then becomes

$$\boldsymbol{S} = \boldsymbol{S'} \circ \boldsymbol{S''} = \begin{pmatrix} S'_{11} + S'_{12}(\mathbb{I} - S''_{11}S'_{22})^{-1}S''_{11}S'_{21} & S'_{12}(\mathbb{I} - S''_{11}S'_{22})^{-1}S''_{12} \\ S''_{21}(\mathbb{I} - S'_{22}S''_{11})^{-1}S'_{21} & S''_{21}(\mathbb{I} - S'_{22}S''_{11})^{-1}S'_{22}S''_{12} + S''_{22} \end{pmatrix}$$

3.4.4 Physical interpretation of the composition of scattering matrices

The formula found above to calculate the scattering matrix for a system composed of two subsystems with known scattering matrices may look cryptic if derived only by algebraic manipulations. Also, matrix inversion is required to compute the composed matrix, so it is not clear whether or not this method overcomes the stability limitations of the transfer matrix technique. In fact, the method works, and its functioning can be understood in terms of the actual physical behavior of the composite system.

The existence of the composite matrix depends on the fact that the matrices $(\mathbb{I} - S''_{11}S'_{22})$ and $(\mathbb{I} - S'_{22}S''_{11})$ are invertible. Consider the first one (the other case is equivalent). If it is singular, then $\det(S''_{11}S'_{22} - \mathbb{I}) = 0$, which implies that $S''_{11}S'_{22}$ has at least one eigenvalue $\lambda = 1$. This condition for the existence of the composed scattering matrix is very strange, and in fact wrong, because unphysical solutions are created.

Consider what happens if there is only one input field a_1 (so $a_2 = 0$). First, the effect of system S' will be that a wavefront $S'_{11}a_1$ is reflected, while $S'_{21}a_1$ is transmitted. If we define $d = S'_{21}a_1$, the transmitted field, d will enter system S'', where a wavefront $S''_{11}d$ will be reflected back. Then, the latter wavefront will enter system S' from the right, and the total reflection to the right will be $S'_{22}S''_{11}d$. The

wavefront just found will undergo the same path as d originally did, and so on. Therefore, the wavefront moving to the right between the systems (a) can be found as:

$$a = d + S'_{22}S''_{11}d + (S'_{22}S''_{11})^2 d + ...$$

Once a is known, then $b_2 = S''_{21}a$. If all of the eigenvalues of $S'_{22}S''_{11}$ are such that $|\lambda_i| < 1$, then we can rewrite

$$\sum_{n=0}^{\infty}(S'_{22}S''_{11})^n = (\mathbb{I} - S'_{22}S''_{11})^{-1}$$

in the same way as the geometric series adds to $1/(1-x)$ if $|x| < 1$. Substituting this result yields

$$b_2 = S''_{21}(\mathbb{I} - S'_{22}S''_{11})^{-1}S'_{21}a_1$$

which is exactly the result found by algebra in the previous section. The three other entries of the composed scattering matrix can be found in the same way and are in agreement with the algebraic derivation.

The condition for the existence of a scattering matrix for the composite system is then that all the eigenvalues of $S''_{11}S'_{22}$ and $S'_{22}S''_{11}$ must satisfy $|\lambda| < 1$. The formula will work if $\lambda \neq 1$, just in the same way as the geometric series for $x = 2$ does not converge but the formula gives a value of -1.

Physically, the condition states that two linear systems described by scattering matrices can be composed in a system described by a scattering matrix if and only if there is no eigen-wavefront that can loop between the systems and increase in magnitude.

The physical picture also sheds light into the stability of the technique with respect to evanescent waves. The inversion just serves as a convenient computational tool to calculate the geometric series of matrices, and in no case reverse propagation is involved. If the evanescent components decay over a roundtrip, which will happen as long as inverse propagation was not included in the component systems, then the resulting matrix will be stable.

3.4.5 Finding eigenmodes

With the ability to compose scattering matrices, the eigenmodes of a system can be found very elegantly and easily. Assume that we are interested in finding the resonant wavefronts on a certain plane in the system for which $z = z_0$. Using the rules for composition it is possible to construct $\boldsymbol{S}'$, the scattering matrix for the portion of the system with $z < z_0$, and also $\boldsymbol{S}''$, the scattering matrix for the part of the system with $z > z_0$.

Suppose that we are interested in the wavefronts moving to the right. If we follow a wavefront u (see figure 3-7), the reflection from the right part of the system can be found from its scattering matrix as $S''_{11}u$. The resulting wavefront will again be reflected by the left part of the system, and come out as $S'_{22}S''_{11}u$.

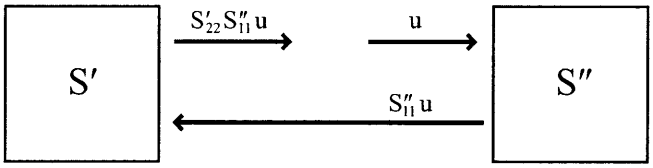

Figure 3-7: Roundtrip transformation of a wavefront in a system.

Finding the resonant modes can then be cast again as an eigenvalue problem:

$$\lambda u = S'_{22}S''_{11}u.$$

The mode finding algorithm using scattering matrices requires more computation to set up than the simpler algorithm of section 3.1, but it allows to calculate the effects on the mode due to multiple reflections, for example in the case of an intracavity element. However, if the extra flexibility is not needed, the simpler algorithm will work well and be much faster.

In order to find the eigenmodes correctly, with either method, it is important to

set up the system so that the portions of the wavefront that get close to the limit of the finite domain get filtered out. This procedure is required to prevent wavefronts to wrap around the system's boundaries due to aliasing, which compromises the correctness of the numerical solution in representing the continuous eigenmodes.

Chapter 4

Design and analysis of the cavity

The proposed cavity consists of a two mirror confocal cavity[1], where the mirror surfaces are limited to a fairly thin ring. This chapter provides some insight in the cavity functioning and also analytical expressions for the parameters of interest and for sizing the mirrors given the separation and wavelength.

Alternative designs were also explored in the past, for examples by designing the profile of the mirror ad-hoc to generate a mode that does not diffract significantly through an aperture ([15]). However, issues of manufacturability and coupling make it so that only spherical mirrors are feasible outside of computer simulations. Furthermore, the solution found using spherical mirrors is extremely satisfactory, so there is no point for designs harder to implement.

4.1 Choice of using a confocal cavity

The first thing that I did after having written the simple eigensolver described in section 3.2 and having tested it successfully on textbook examples was to model a simple cavity with a fairly tight focus and a small hole in the mirror, assuming no angular dependence of the eigenmodes. For such a system, the losses per roundtrip of the best mode[2] are fairly high unless the size of the aperture is kept really small,

[1]The separation of the mirrors equals their radius of curvature.

[2]For brevity, I will refer to the mode with the least losses as the *best mode*.

as noted in other studies (see chapter 1).

To have an idea of the parameter space, and as a good way of testing the solver, the variations in roundtrip loss were explored by varying the radius of curvature, the wavelength and the separation between the mirrors. Varying the first two parameters did not result in surprises. However, varying the cavity length gave a result with lots of structure. Figure 4-1 shows the fraction of the energy[3] that is retained after one roundtrip by the best mode in a cavity with $R = 20$ cm constructed with 1/2 inch mirrors having an aperture with a diameter of 1 mm and driven with a field at $\lambda = 2\mu$m.

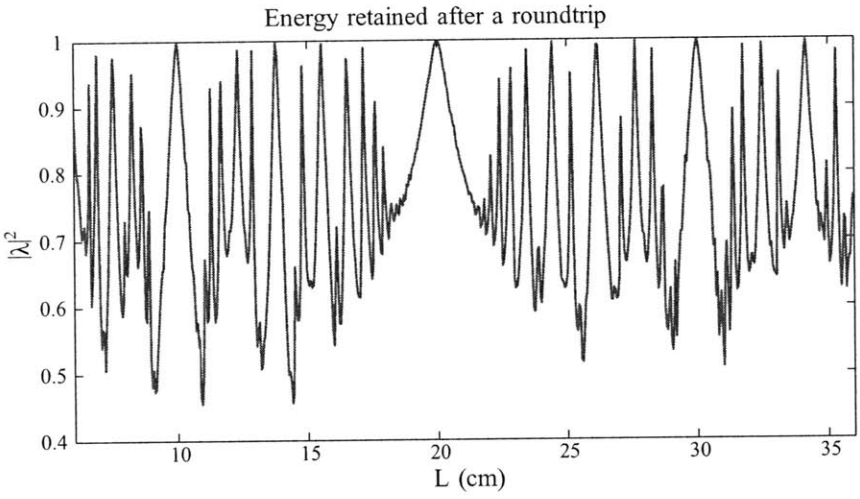

Figure 4-1: Fraction of the energy left after one cavity roundtrip for the least lossy resonant mode as the distance between the mirrors is varied.

It is immediately clear that there are certain values of L for which having an aperture does not introduce significant loss. The most evident value corresponds to the case of a confocal cavity ($L = R$), and the two next prominent peaks occur for $L = R/2$ and $L = 3R/2$. There are many other peaks, but they are all very narrow and most of them have visible losses. For alignment reasons, it is encouraging that the fractional loss curve (simply $1 - |\lambda|^2$) has quadratic behavior in proximity of the three points mentioned.

If the cavity needs to have a hole of relatively large size, it is imperative that it

[3]Or in other words $|\lambda|^2$ in terms of the eigenvalue.

is operated near a peak. The loss calculated for figure 4-1 is in the case of perfectly reflecting mirrors, and it is entirely due to diffraction directing energy out of the cavity either through the hole or off the sides. This loss of energy can be seen as an increased transmissivity in equation 2.16, leading to a decrease in enhancement. Since cavity enhancement is crucial to be able to reach critical intensities for HHG, it is not acceptable to have a cavity limited by design to have low finesse.

To understand the nature of these resonances that can withstand the presence of an aperture without experiencing losses, we can look at equation 2.17 which gives the frequency of a cavity mode (for a cavity with no holes) given its quantum numbers in rectangular coordinates. In the case of a CW laser, the cavity is excited only at a single frequency, so only the modes for which

$$f_{mnq} \approx f_{laser}$$

can be excited.

The amount of modes that can be excited at a certain cavity length is determined by the factor

$$\cos^{-1}\left(1 - \frac{L}{R_0}\right).$$

Suppose that the factor is an irreducible fraction of π of the form $a\pi/b$, then the frequency of the modes reduces to

$$f_{mnq} = \frac{c}{2L}\left[q + (m+n+1)\frac{a}{b}\right],$$

meaning that all the modes for which $bq + a(m+n+1)$ is a constant integer can be excited.

It is clear that not all transverse modes are accessible with a single frequency. Suppose that the mode for $m = n = 0$ can be reached for a certain cavity and a certain laser, and that such mode has $q = q_0$. The next excitable mode for either m or n is such that

$$b \cdot \Delta q + a \cdot \Delta m = 0$$

which can be solved for the smallest integers giving $\Delta m = b$ and $\Delta q = -a$.

Knowing that the mode (m_0, n_0, q_0) can be excited, it follows that also the modes with quantum numbers

$$(m_0 + ib, n_0 + kb, q_0 - (i + k)a),$$

given integers i and k, can be excited with the same setup.

The more modes that are accessible (of the traditional cavity without apertures), the better the cavity can withstand the presence of an aperture without losses. This property is due to the fact that all the Hermite-Gaussian modes that can be excited are in fact part of the same degenerate space, so it is possible to superpose them in any way to get another eigenmode with the same eigenvalue. The more basis vectors that are available, the more flexibility we have in generating arbitrary wavefronts by superposition. In particular, if the basis set is close to being complete, it is possible to create a new eigenvector by superposition which has extremely low field amplitude in the location where the aperture is.

In the ideal case it would seem that $a/b = 1$, so the entire set of Hermite-Gaussian modes can be accessed. However, this condition corresponds to $L = 2R_0$, a cavity with a really tight focus at the limit of stability. The reason why this kind of cavity would work very well in the presence of holes can be understood from ray optics. All the rays pass through a single focal point, and the mirror surfaces are both on the same spherical surface centered around the focus. A single ray will bounce back and forward along a diameter of the sphere, intersecting it always at the same two points. Therefore all those rays for which both of the points are on the mirror surface (not on the aperture) will be stable.

In the case where the system is forced to have circular symmetry though, the entire set of Hermite-Gaussian modes is not needed, since the corresponding Laguerre-Gaussian modes can be constructed by using either all-even or all-odd m and n[4], so

[4]The parity of m and n can differ, but all the HG components will have the same parity for m and n. For example,

$$LG_{10} = -\frac{HG_{02} + HG_{20}}{\sqrt{2}}$$

effectively the case where $a/b = 1/2$ is enough to have a complete basis. This is the case for the confocal cavity, where $L = R_0$. The physical reason for needing only half of the modes is that any mode with circular symmetry and even angular dependence has to be constructed only of modes that are inversion symmetric[5], while any mode with circular symmetry and odd angular dependence has to be constructed of modes antisymmetric with respect to inversion.

When $L = R/2$, $a/b = 1/3$, and when $L = 3R/2$ $a/b = 2/3$, so the transverse modes accessible are one out of three in each dimension. When $L = R(1 \pm 1/\sqrt{2})$, the accessible modes are one out of four in each dimension[6], and so on. Each length for which the inverse cosine factor is a fraction of π will be a peak in the graph of figure 4-1.

The choice of the confocal cavity stems from its property of supporting a complete basis of eigenmodes, therefore giving it the best rejection to losses due to apertures and the highest tolerance for imprecise alignment. Furthermore, the $L = 3R/2$ cavity has a double focus, while the $L = R/2$ presents no significant advantage over the confocal cavity and has a tighter tolerance for alignment.

4.2 Single-mode operation

Since the resonances that are stable when apertures are introduced arise from the fact that the modes are degenerate, these kind of cavities also have the downside of supporting many modes all of which are excitable. Mode degeneracy is unwanted in a resonator, because of inter-mode coupling occurring due to scattering and nonlinearities which brings the cavity in unwanted and unexpected regions of operation, with not well-characterized spatial properties of the focus and also a bad intensity and phase profile due to beating.

---

while

$$LG_{13} = \frac{3}{4}HG_{14} + \frac{1}{2\sqrt{2}}HG_{32} - \frac{\sqrt{5}}{4}HG_{50}.$$

The derivation of the formulas for conversion between the two basis of modes can be found in [14].

[5]With respect to the origin.

[6]Notice the resonance corresponding to $L = R(1 + 1/\sqrt{2})$ in figure 4-1 at $L \approx 34.14$ cm.

In the case of the designed cavity, there are actually two degenerate modes that survive due to the geometry of the resonator, but they are a pair of symmetric and antisymmetric modes that for all practical coupling techniques will be equally excited in a reliable way, as will be analyzed in section 4.2.4.

4.2.1 Single mode operation in a degenerate cavity

Ideally, the cavity should support only a single mode at a given laser frequency. In the case of a cavity with degeneracy though, it is nearly impossible to achieve pure, single mode resonance, so what we really care about is the fact that one of the mode dominates over the others.

If each mode is excited equally by the external laser field, their intensity enhancement is proportional to

$$\frac{1}{(1-R)^2},$$

from equation 2.15, assuming zero roundtrip phase. The squared quantity, in the context of a cavity with losses is simply half of the roundtrip losses[7], so the resonance boosts the intracavity mode power by a factor of

$$\frac{4}{L^2}, \tag{4.1}$$

where L is the total roundtrip power loss, compared to the power that will be transmitted through a single mirror.

Therefore, if the fractional loss of the eigenmode u_1 is L_1, and the fractional loss of eigenmode u_2 is L_2, the ratio of their intracavity powers will be

$$\frac{P_1}{P_2} = \frac{L_2^2}{L_1^2}.$$

If there is a single mode u_b for which given any other mode u_i

$$\left(\frac{L_i}{L_b}\right)^2 > K_r,$$

[7]Which are $\approx \frac{1}{2} \cdot 2T = (1-R)$ if the cavity has no losses and the reflectivity is reasonably high.

then if we couple equal amounts of power with equal coupling efficiencies in the cavity for all modes, the circulating power in mode u_b is going to be a factor of K_r higher than in the other modes. If a value of K_r can be found for which the cavity behavior is practically single mode for the intended application, then the problem with degeneracy is solved.

Fairly good mode separation can occur even if the roundtrip energy change is very similar because of the quadratic dependence. If one mode retains 99% of its power, while another retains only 95%, the first one will have a circulating power approximately 25 times higher. It is crucial that L takes in account the power lost due to transmission through the mirrors as well, usually an additive factor of $2T$ for high reflectance mirrors and low loss modes.

It is important to keep in mind that the enhancement factor of equation 4.1 is purely that of the mode's wavefront once it is already inside of the cavity. The overall enhancement from the coupled portion of driving beam depends also on the mirror reflectivity as shown in equation 2.15. For a given mode, the total enhancement factor becomes smaller as the intracavity losses lower the finesse:

$$\frac{|E|^2}{|E_0|^2} \approx \left|\frac{t}{L/2}\right|^2 \approx \frac{T}{(T+L_0/2)^2} \approx \frac{1}{T}\cdot\frac{1}{\left(1+\frac{L_0}{2T}\right)^2}$$

where L_0 is the amount of losses not due to the transmissivity of the mirror. When the extra losses amount roughly to $0.82T$, the enhancement factor is reduced by a factor of 2. Since one of the goals of the cavity is to produce enhancement, it is a good idea to limit the losses of the chosen mode to be less than half of those due to one reflection at the mirror.

Furthermore, at least the mirror through which light is coupled in should be nearly lossless, otherwise the enhancement is further reduced, while the other mirror could ideally have $R = 1$. If it is the case[8], then the overall power enhancement becomes

$$\frac{4T}{(T+L_0)^2} = \frac{4}{T}\cdot\frac{1}{\left(1+\frac{L_0}{T}\right)^2}.$$

[8]Real dielectric mirrors are very close to this ideal case.

In light of the above expression, the maximum enhancement is limited by losses to $1/L_0$ when $T = L_0$.

4.2.2 Traditional ways of limiting degeneracy

Two common methods to force operation at a non-degenerate point are the introduction of an aperture in the cavity and the operation slightly off the degeneracy.

The usual way to force lasers to radiate in a single mode is to include an aperture at the center of the cavity, introducing high losses in the high order modes and allowing for lasing mainly at the fundamental gaussian mode.

Simulating on the computer the iris at the center of the cavity, and varying its aperture size gave the plot of figure 4-2. Unfortunately, the roundtrip loss is at around 5% before the mode degeneracy starts to break, leading to a maximum theoretical enhancement of around 20.

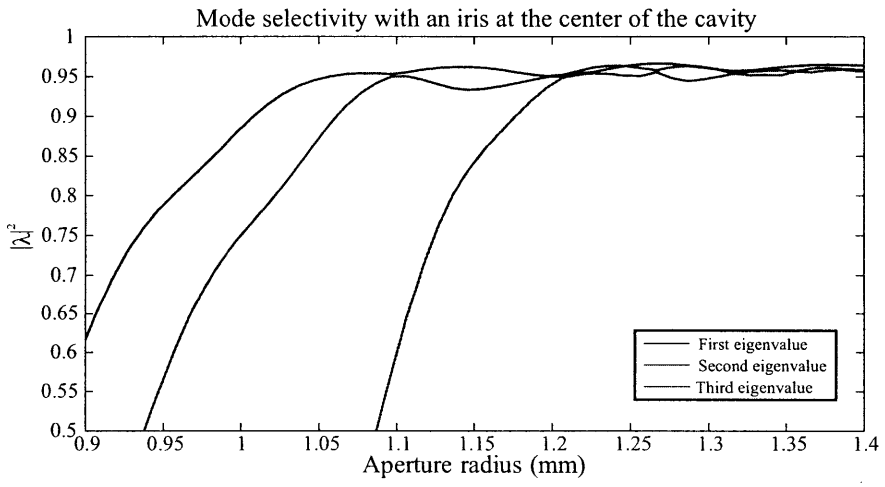

Figure 4-2: Mode selectivity when an iris is placed at the center of the cavity.

Another way of breaking the degeneracy is that of moving the mirrors slightly off the confocal configuration, so that one mode will survive more than the others as the degeneracy is broken. The result of simulating this method on the computer is shown in figure 4-3. Unfortunately the modes do not separate enough from each other to be able to achieve effective single-mode operation.

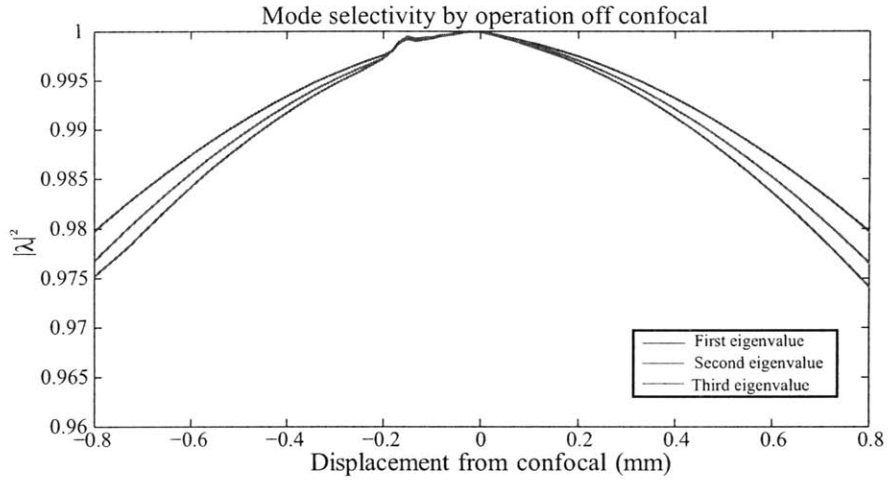

Figure 4-3: Mode selectivity obtained by displacing the mirrors from confocal configuration.

4.2.3 Restriction of the mirror size

A third approach that I tried was to restrict the size of the mirror. Suppose that the dimensions of the hole have already been decided, then it is possible to size the outer radius of the mirror so that only a ring is left. By reducing the thickness of the ring appropriately, it should be possible to get to the point where the complete but bandlimited basis of modes can be superposed only in one way such that the losses are small.

An analytical formula to determine the optimal mirror width

Let us define a few fundamental variables for the design of the cavity. Let R be the radius of curvature of the mirrors, r be the average radius of the ring-shaped mirror, Δr be the thickness of the ring and λ be the wavelength of the driving laser. Refer to figure 4-4.

Assuming that $r \ll R$, $\theta \approx 2\Delta r/R$. If two plane waves were to propagate at an angle θ with respect to each other, the spatial period of their interference pattern will be

$$\frac{\lambda}{2\sin\theta}.$$

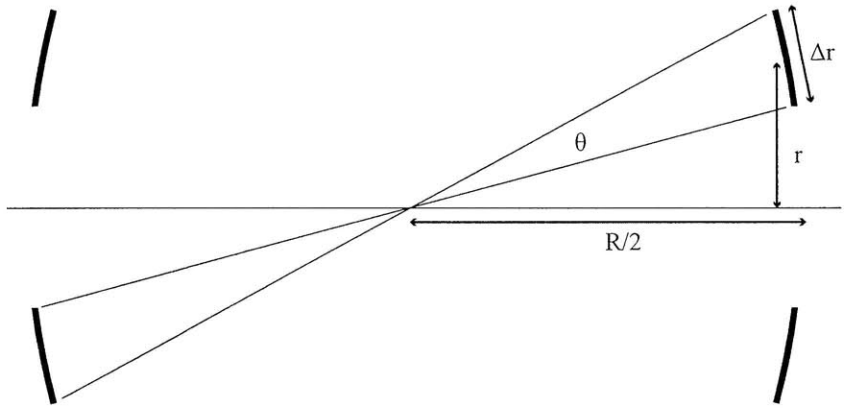

Figure 4-4: Naming of the variables determining the geometry of the cavity.

It is reasonable to assume that if Δr is proportional to the pitch of the interference of the two plane waves above, then the cavity will practically operate in single mode. The exact constant of proportionality is hard to compute from first principles, and it depends also on what mode separation is considered acceptable. Leaving the numerical solver with the task of finding the constant of proportionality, an analytic expression can be derived in the paraxial case for determining the dependence of Δr on the other parameters:

$$\Delta r = \frac{\lambda}{2\sin\theta} \approx \frac{\lambda}{2\theta} \approx \frac{\lambda}{2 \cdot \frac{2\Delta r}{R}} = \frac{\lambda R}{4\Delta r},$$

from which it follows that

$$\Delta r \sim \sqrt{\lambda R}. \tag{4.2}$$

Numerical computations

While the above physical reasoning gives an approximate functional form for the point where modes start to get a considerable loss, in principle it is hard to tell whether the modes will separate in a convenient way, or all of them will equally get more lossy.

It is possible to use the computer to analyze the loss of the resonant modes as the thickness of the ring is varied, as well as test numerically equation 4.2 and in case find a suitable constant of proportionality.

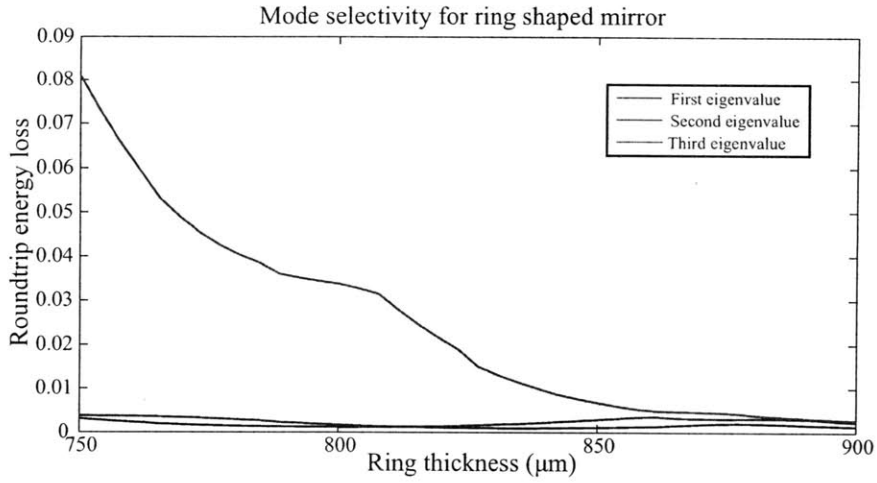

Figure 4-5: Mode selectivity obtained by varying the extent of the mirror surface, shaped as a circular ring.

The results for a 20 cm cavity with $r = 1.5$ mm driven at 1 μm are shown in figure 4-5. When compared to the two common techniques, reducing the mirror size is able to achieve a sharp separation of the first two modes from the other ones.

Given the fact that the roundtrip losses for the first two modes are in the neighborhood of half a percent, the optimal power reflectance of the mirrors is at around 99%. As a reasonable target value for the attenuation of the third mode, I choose 5% per roundtrip. The numerically found curve for the loss of the third mode of figure 4-5 attains the desired value for a thickness of 768 μm, which can be used to evaluate the constant of proportionality to be very close to 1.72 (which in turn is very close to $\sqrt{3}$, to keep the formula simple). For a third mode loss of 5% then, the thickness of the ring is given by[9]:

$$\Delta r \approx \sqrt{3\lambda R}. \tag{4.3}$$

It is also possible to use the computer to check the correctness of equation 4.3 for its dependence from the cavity parameters R, r and λ. I used the software to sweep through a range of values for the parameters, while evaluating the eigenvalues at ten

[9]If the target attenuation is different, the constant will differ, but only by a small factor. From figure 4-5 it is possible to notice how over a $\sim$ 12% fractional variation of Δr the third mode loss goes from 1% to 8%.

different values for Δr centered around the expected result from the analytic formula and spanning 150 μm. The ring thickness for which the third mode losses reach 5% was then estimated from the ten datapoints using MATLAB's standard piecewise cubic interpolation.

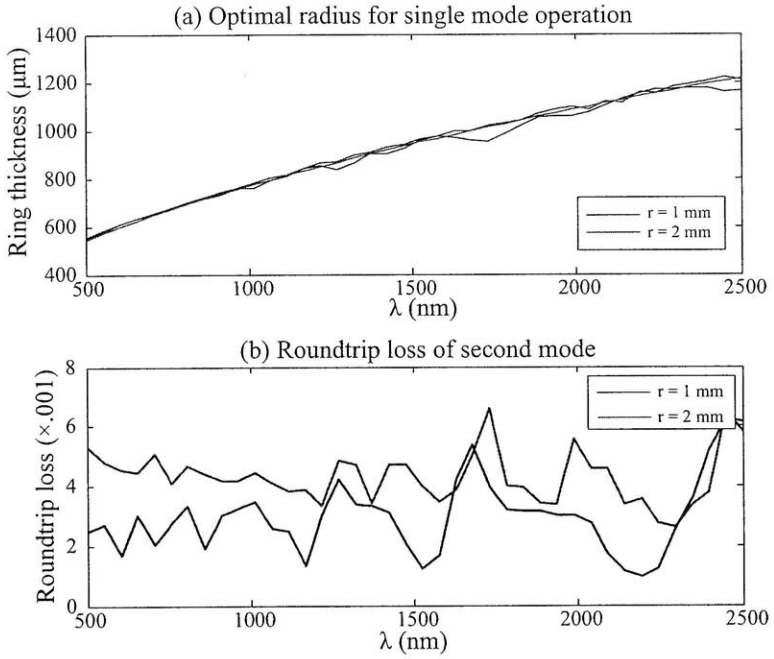

Figure 4-6: Single mode cavity as λ is varied. (a) Δr to achieve single mode operation (together with the analytic expression), (b) roundtrip losses of the second mode.

Using this technique, the dependence of Δr on λ was analyzed numerically (see figure 4-6). For a cavity with $R = 20$ cm and for r being 1 or 2 mm, the required ring thickness predicted by equation 4.3 is very close to what determined numerically for λ between 500 nm and 2.5 μm. The losses of the first two modes are also below 0.7% for all the cases, and below 0.4% for $r = 1$ mm and $\lambda < 1200$ nm.

In figure 4-7, Δr is determined for a cavity with $r = 1.5$ mm driven at $\lambda = 1$ μm for R between 10 and 40 cm. The ring thickness again behaves as predicted, but the losses of the second mode, below 0.4% for $R > 15$ cm, increase substantially for values of the curvature under 15 cm. More careful analysis indicates that it is not a numerical artifact, so this result might indicate that this kind of cavity can operate

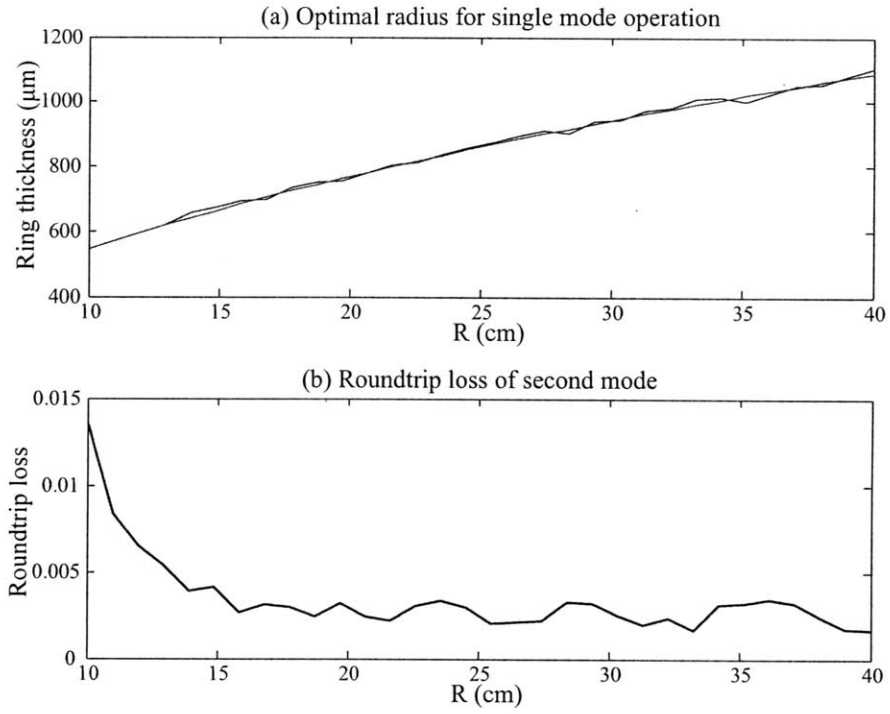

Figure 4-7: Single mode cavity as R is varied. (a) Δr to achieve single mode operation (together with the analytic expression), (b) roundtrip losses of the second mode.

as intended only for $r < R/100$.

Finally, the variation of Δr with respect to r is shown in figure 4-8, for a cavity with $R = 20$ cm and driven at $\lambda = 1$ μm. As expected, the radius for single mode operation is insensitive to changes in the ring mean radius, and it deviates less than 20 μm from the reference level; the losses stay below 0.4%.

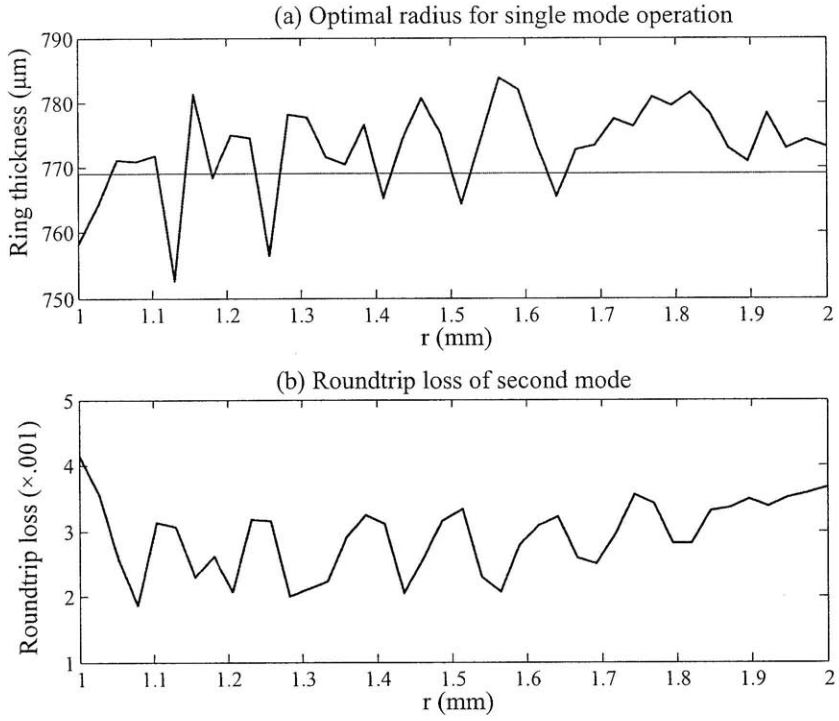

Figure 4-8: Single mode cavity as r is varied. (a) Δr to achieve single mode operation (together with the analytic expression), (b) roundtrip losses of the second mode.

Considerations for the enhancement of ultrafast pulses

Confocal cavities are very broadband structures, however by forcing pseudo single-mode operation via ring shaped mirrors bandwidth is reduced. If the cavity is designed for a particular wavelength λ_0, then the components with $\lambda < \lambda_0$ will see reduced losses for the transverse modes beyond the first two, reducing the effective single-mode operation. If $\lambda > \lambda_0$, then eventually the first two modes will start to experience

losses.

From figure 4-6, it looks like it is possible to get about 100 nm or more of bandwidth in the Ti:Sapphire window, while maintaining a sufficient enhancement factor for HHG and fair mode separation.

4.2.4 Structure of the two dominant modes

As mentioned earlier, it is actually impossible to limit the cavity to resonate in one single mode, and two modes will always have similar losses[10]. By using the software, it is possible to visualize the spatial field distribution inside of the cavity for the two modes of interest. The result of simulating the propagation and reflection of the modes' wavefronts is shown in figures 4-9 and 4-10. Let us denote these modes by u_1 and u_2, respectively.

These plots represent the magnitude of the complex field for a roundtrip in a 20 cm long cavity with $r = 2$ mm and $\lambda = 2$ μm. The wavefront starts immediately after a mirror at $z = 0$, then propagates through the cavity and gets reflected at $z = 20$ cm by the second mirror, and finally comes back where it started.

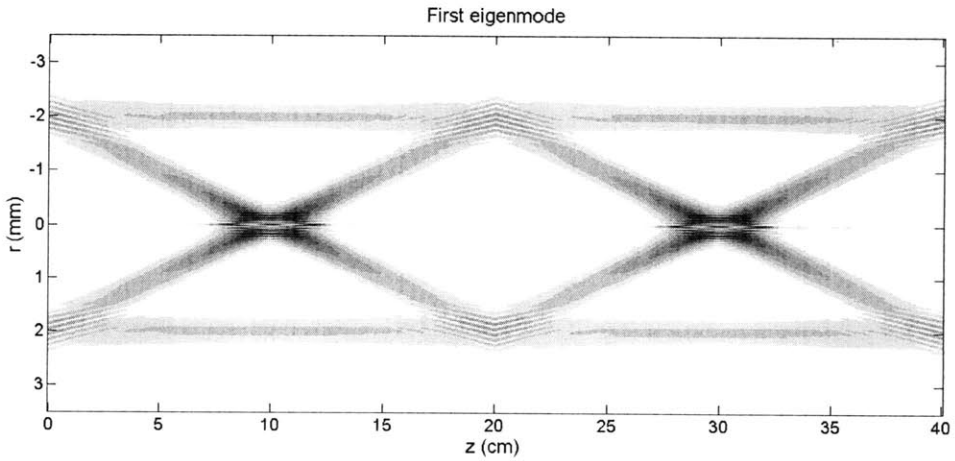

Figure 4-9: Magnitude of the complex field of the first mode (u_1).

The two modes appear almost identical, but they differ by the relative phase of the straight section with respect to the crossed section, as it is possible to notice

[10]In fact, even the more lossy modes come in pairs, but we are not interested in them.

by examining the interference patterns in proximity of the mirrors (the fringes are shifted between the two modes). Even though the different interference pattern at the mirrors produce slightly different eigenvalues, due to the fact that some of the field on the sides is not reflected, the two modes are practically degenerate.

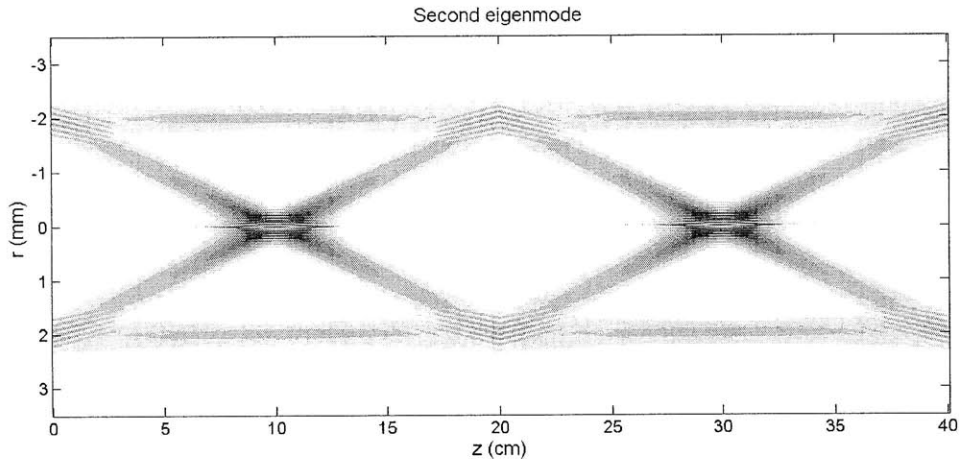

Figure 4-10: Magnitude of the complex field of the second mode (u_2).

Any linear combination of the two modes is then itself a low loss mode, so it is possible to combine them in a more convenient way. In figures 4-11 and 4-12 are shown the field distribution of modes $\psi_1 = (u_1 + u_2)/\sqrt{2}$ and $\psi_2 = (u_1 - u_2)/\sqrt{2}$.

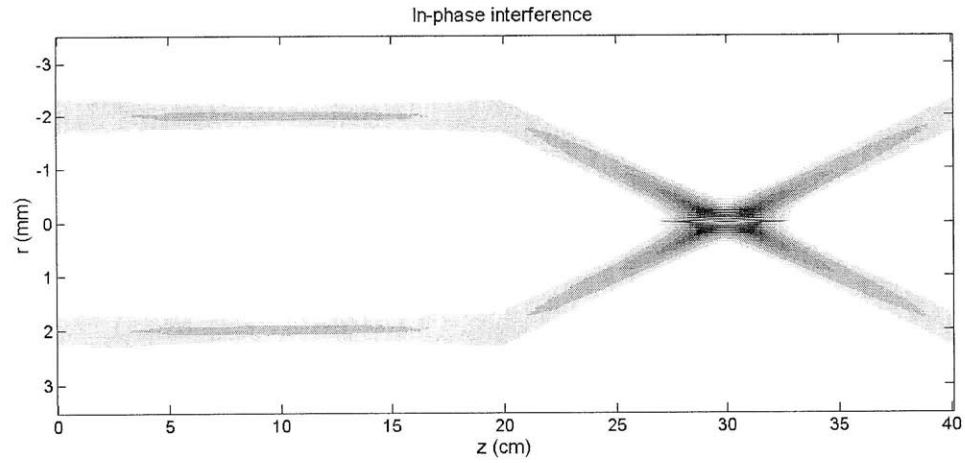

Figure 4-11: In phase addition of the first two modes (ψ_1).

The structure of these modes is clear from the ray picture: for ψ_1, light travels straight up to the first mirror, which focuses it in the center of the cavity, imaging

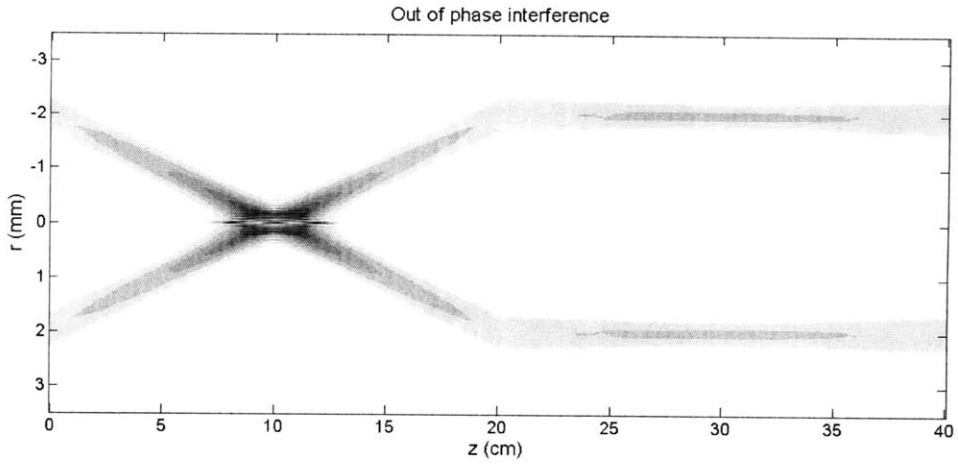

Figure 4-12: Out of phase addition of the first two modes (ψ_2).

it exactly on the other mirror[11]. ψ_2 is exactly the same, except that light is initially focused, and then the return path is straight.

The behavior of ψ_2, shown in figure 4-13, is convenient for HHG. Assuming that the laser pulse is coupled in from the left, it is focused on the forward path, so the generated harmonics can leave the cavity from the other side, where there is no coupling optics.

It is possible to excite almost exclusively ψ_1 or ψ_2 by entering the cavity with a ring shaped beam that goes initially straight or that focuses, respectively, therefore in practice it is possible to operate this cavity in a single mode, which was our goal.

4.3 Analysis of the focus

So far, we showed that it is possible to design a cavity with large apertures which allows for a pulse energy enhancement factor of around 100. While it certainly helps, it is still not sufficient to achieve HHG. The limitation is that a good dielectric mirror can withstand instantaneous intensities[12] of about 10^{12} W/cm^2, therefore the driving pulses are limited to have a peak intensity of about 10^{10} W/cm^2 right before the mirror. To achieve the intensities required by HHG, the cavity needs necessarily to

[11]Notice how the imaging condition is satisfied from a mirror to itself, since the if f is the focal length of the mirrors, the cavity is $2f$ long so $1/2f + 1/2f = 1/f$

[12]Only for ultrashort pulses that do not induce thermal damage.

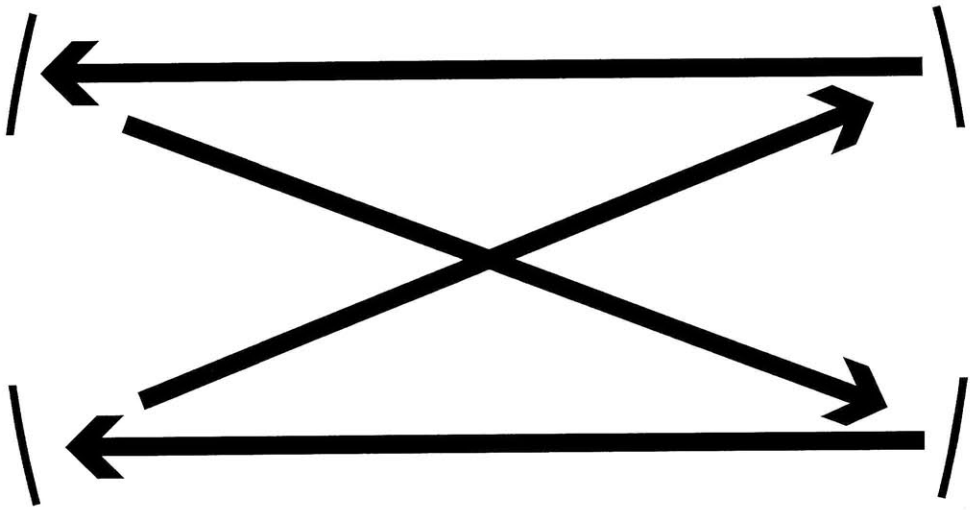

Figure 4-13: Direction of wave propagation for ψ_2.

focus the light very strongly.

To calculate the intensity gain from the mirror's surface to the focus[13], let us first calculate the size of the focal region, shown in figure 4-14. In the paraxial approximation, we have that $L \sin 2\theta = \Delta r$. Therefore the transverse size of the focal region is

$$r_{center} \sim \sqrt{\lambda R}$$

while the longitudinal extent is

$$l_{focus} \sim 2L\cos\theta = 2\frac{\Delta r}{\sin 2\theta}\cos\theta \approx \frac{R\Delta r}{r} \sim \frac{\lambda^{1/2}R^{3/2}}{r}$$

The ratio of the area of the ring to that of the focal region is proportional to

$$\frac{r\Delta r}{r_{center}^2} = \frac{r}{\Delta r},$$

which for the cavities considered so far is a small value. However, this ratio does not

[13]This derivation is aimed only to find the functional form of the expressions for spot size and gain. The constant factors will be calculated from computer simulations.

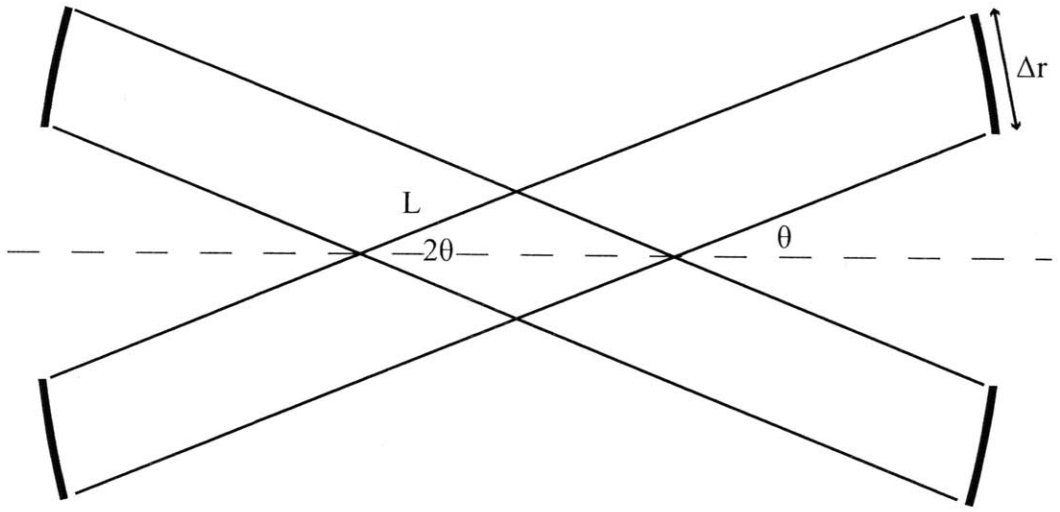

Figure 4-14: Calculation of the size of the region of focus.

constitute the gain, because the focus has additional structure due to interference, as shown in figure 4-15.

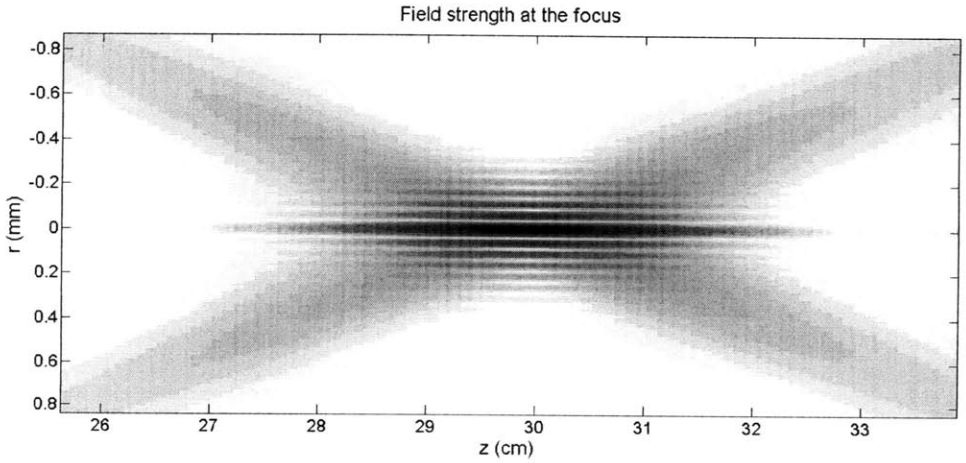

Figure 4-15: Field strength at the focus.

the width of the central fringe can be related to the width of the interference pattern of plane waves incident with angle $2\theta \approx 2r/R$, so that in the paraxial approximation

$$r_{focus} \sim \frac{\lambda R}{r}.$$

To determine the gain, it is not sufficient to take the ratio of the ring area to the

focus transverse area, since there is a non-negligible amount of energy in the fringes surrounding the central interference peak.

Since the focal region is approximately formed by the superposition of plane waves whose $\boldsymbol{k}$ vector makes a constant angle with respect to the axis of propagation, the Hankel transform tells us that the spatial pattern must be very similar to a truncated Bessel beam.

The envelope of a Bessel function goes as $1/\sqrt{r}$, so the differential energy per radial increment is

$$\mathrm{d}E = 2\pi r|u|^2\mathrm{d}r \sim \mathrm{d}r.$$

This result means that the fraction of the energy in the central peak is proportional to the ratio of its radius to the radius of the entire focal region, so the cavity gain can be expressed as

$$g = \frac{A_{ring}}{A_{focus}} \cdot \frac{r_{focus}}{r_{center}} \sim r\sqrt{\lambda R}\frac{r^2}{\lambda^2 R^2} \cdot \frac{\lambda R}{r}\frac{1}{\sqrt{\lambda R}} = \frac{r^2}{\lambda R} \tag{4.4}$$

Numerical testing for equation 4.4 has been performed for the same cavity parameters as in the previous section, and the results are shown in figures 4-16, 4-17, and 4-18.

As before, the functional form of equation 4.4 is verified, and numerical constants can be estimated for gain and spot size to be:

$$g \approx 119.2 \cdot \frac{r^2}{\lambda R}$$

$$w_0 \approx 0.177 \cdot \frac{\lambda R}{r}.$$

Therefore, this kind of cavity allows for an intensity gain of three orders of magnitudes, reaching intensities compatible with high harmonic generation at the focus, while not damaging the mirrors.

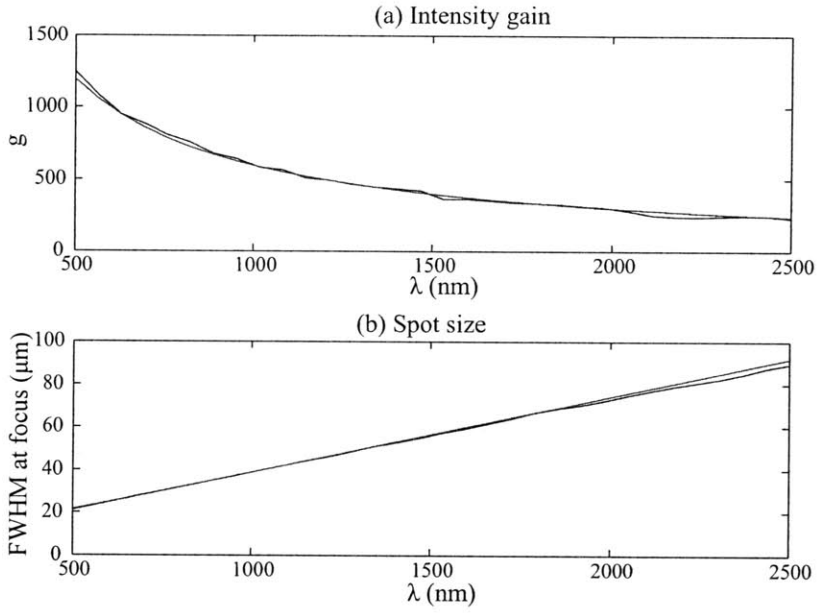

Figure 4-16: (a) gain and (b) spot size dependence on λ, together with the analytic expressions.

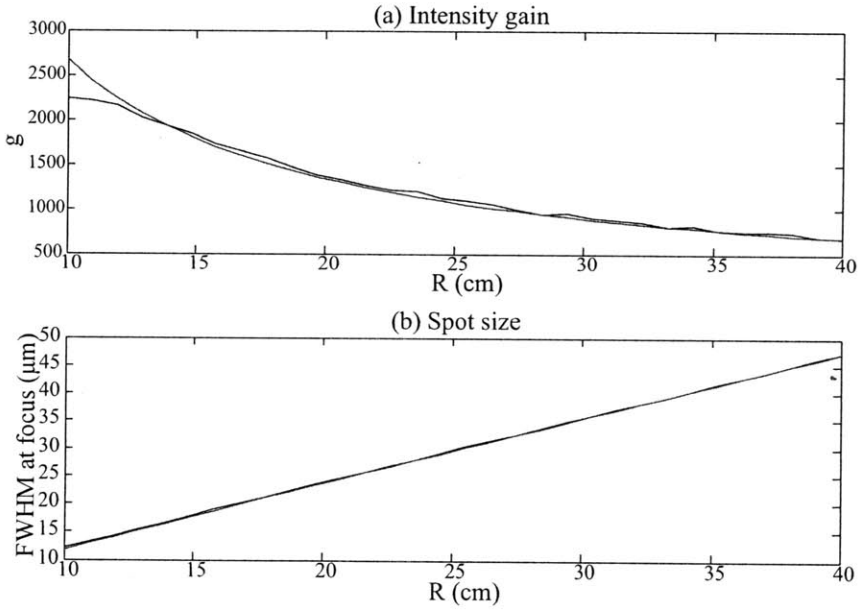

Figure 4-17: (a) gain and (b) spot size dependence on R, together with the analytic expressions.

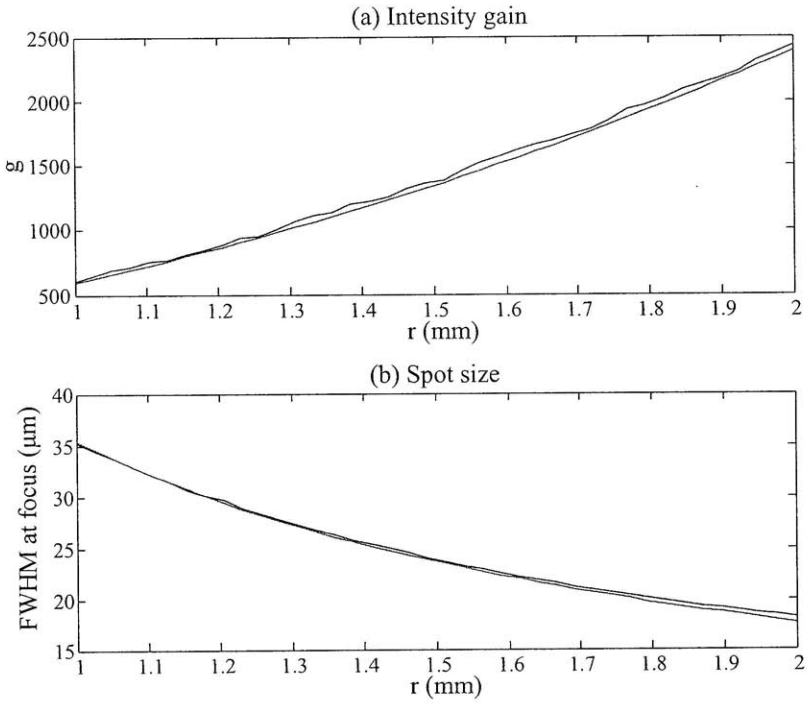

Figure 4-18: (a) gain and (b) spot size dependence on r, together with the analytic expressions.

4.4 Coupling of external fields

The disadvantage of the proposed cavity design is that the coupling efficiency of a regular gaussian beam is extremely low, due to the fact that either most of the beam power is located where the aperture is, or the beam is expanded so much that most of the power lies outside of the ring mirror.

Even considering the large gain and the power enhancement, for the cavity to be practical external fields need to be coupled in fairly efficiently. Given the mode structure, a good way of coupling the laser into the cavity is to transform the beam to have a ring shape, which can be done by using an axicon[14].

The idea is to use the axicon to convert a gaussian beam into a ring shaped beam which is then coupled into the cavity at the right angle with the help of two lenses, as shown in figure 4-19. Even though other combinations of lenses' focal lengths and distances can produce the right coupling angles for a single ray, the $4f$ combination also ensures that the ring's wavefronts themselves are not diverging.

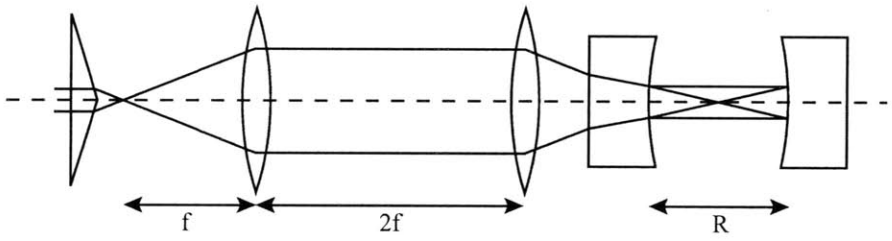

Figure 4-19: Proposed coupling scheme, using an axicon.

Given the length of the resonator R and the angle of the axicon α', the average radius of the mirror ring can be determined geometrically. Referring to figure 4-20, call α the angle $(\pi - \alpha')/2$. For an incoming ray perpendicular to the axicon's flat face, the conical surface's normal will be at an angle α with respect to the z-axis, so

[14]Also, the mode at the focus is very similar to a truncated Bessel beam, which can be created using an axicon.

(assuming that all the angles are small)

$$\alpha + \gamma = n_a \alpha,$$

where n_a is the refractive index of the axicon, so that the angle of the ring beam is

$$\gamma = (n_a - 1)\alpha. \tag{4.5}$$

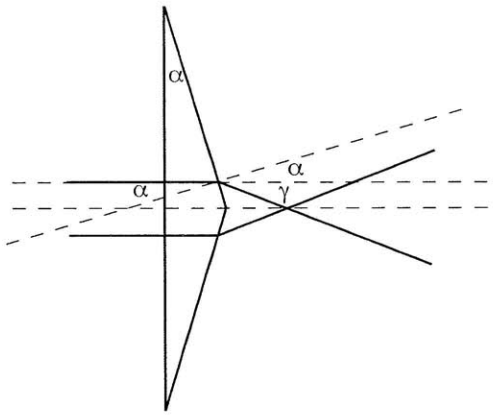

Figure 4-20: Angle of ring-shaped beam.

The lens system makes it such that the incident angle at the mirror will be γ, as shown in figure 4-21. The angle inside the substrate of refractive index n_m will then be γ/n_m. If the angle of the beam inside the cavity is denoted by β, then the surface normal at the mirror is $\beta/2$, and Snell's law gives the relation between γ and β as

$$\frac{\beta}{2n_m} = \frac{\gamma}{n_m} - \frac{\beta}{2},$$

which can be rewritten as

$$(n_m + 1)\beta = 2\gamma. \tag{4.6}$$

Putting together equations 4.5 and 4.6, the angle inside the cavity can be calculated from α directly:

$$\beta = 2\frac{n_a - 1}{n_m + 1}\alpha.$$

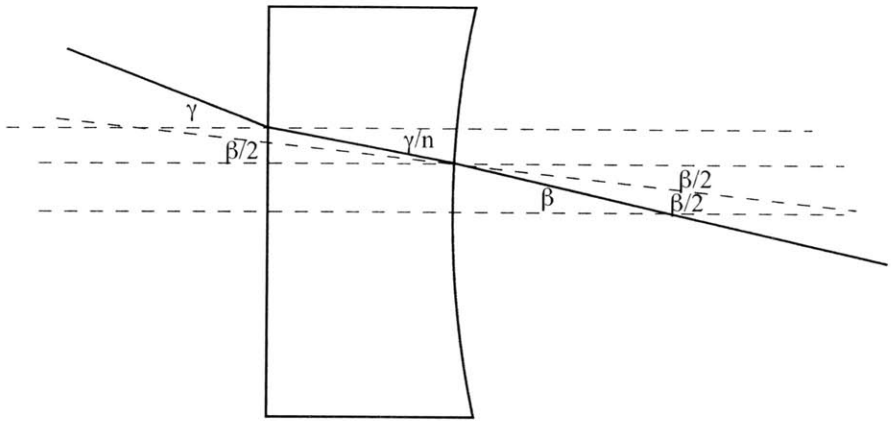

Figure 4-21: Beam angles in refraction from the mirror's substrate.

The mean radius of the ring mirror surface can then be calculated to be

$$r = \frac{n_a - 1}{n_m + 1}\alpha R.$$

Using the computer, this coupling scheme was simulated for a cavity with $R =$ 15 cm, $\lambda = 633$ nm, $\alpha' = 175°$ and $f = 10$ cm, for mirrors with 99% power reflectance[15]. The refractive indices were taken to be both 1.52. The mirrors were assumed to be fully transparent in the regions outside of the ring.

The cross sectional field strength is shown in figure 4-22, and it is in accordance with the ray-optics picture. The total beam power and the peak intensity are shown in figure 4-23. The overall intensity gain from the initial gaussian beam to the cavity focus is $g = 4404$, for a waist size of 200 μm.

This means that to reach an intensity of 10^{15} W/cm^2, the gaussian's peak intensity needs to be around 2.5×10^{11} W/cm^2, and so have a peak power of about 300 MW. If we assume a pulse width of 25 fs, the total pulse energy required for HHG will be around 8 μJ.

Approximately 68% of the incident power leaves the cavity from the rightmost mirror, therefore even with relatively simple coupling optics the coupling coefficient can be fairly high.

[15]These parameters were used because a possible test cavity could be made from such components.

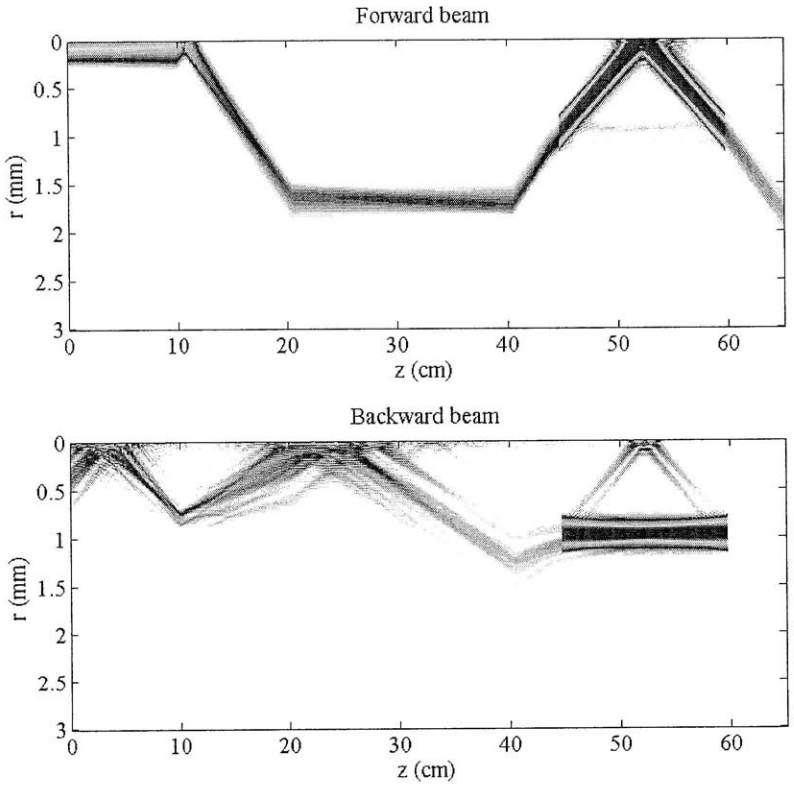

Figure 4-22: Field strength in both directions for the cavity and the coupling optics.

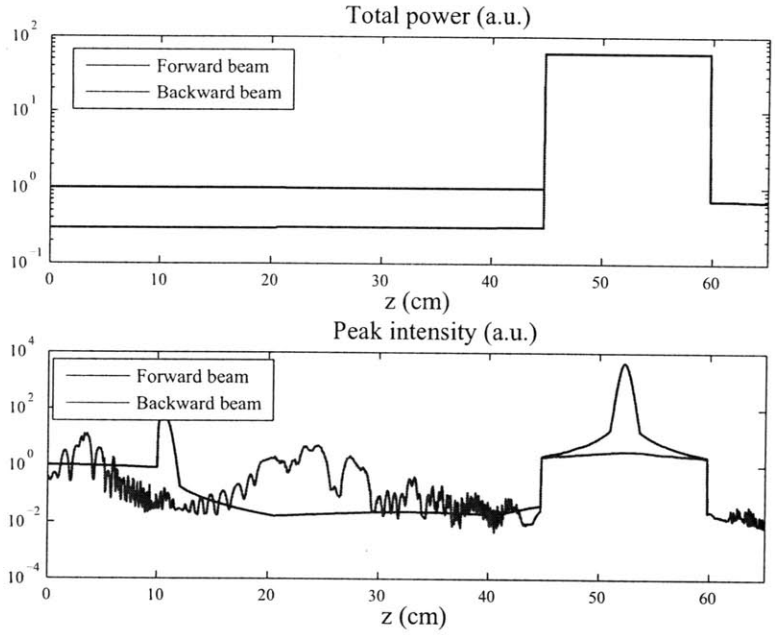

Figure 4-23: Plot of the total power and peak intensity in the forward and backward propagating waves.

4.5 Phase matching

A factor affecting the maximum interaction length of the laser pulse with the gas jet is the length of the region where quasi phase-matching can be achieved. The proposed cavity design has a linear Guoy phase shift at the focus, due to the fact that the beam structure is similar to a Bessel beam.

Given the angle $\theta = 2r/R$, then the phase shift with respect to a plane wave per unit length is given by

$$\frac{\mathrm{d}\phi}{\mathrm{d}z} = k_z - k_0 = -k_0(1 - \cos\theta) \approx -k_0 \frac{2r^2}{R^2}. \tag{4.7}$$

The phase shift is negative, since the phase velocity along the z-axis is never less than the speed of light.

In the case of a 20 cm cavity with $r = 2$ mm and $\lambda = 2$ μm, the predicted phase shift rate of change is $2\pi \times 10^2$ rad/m. Using the computer, it is possible to calculate the phase difference with a plane wave for a series of closely spaced points along the

z-axis, and then unwrap the angle. The result is shown in figure 4-24; evaluating the slope between $z = 9$ cm and $z = 11$ cm gives a variation in phase shift per unit length of 630.9 rad/m, extremely close to the predicted value from equation 4.7.

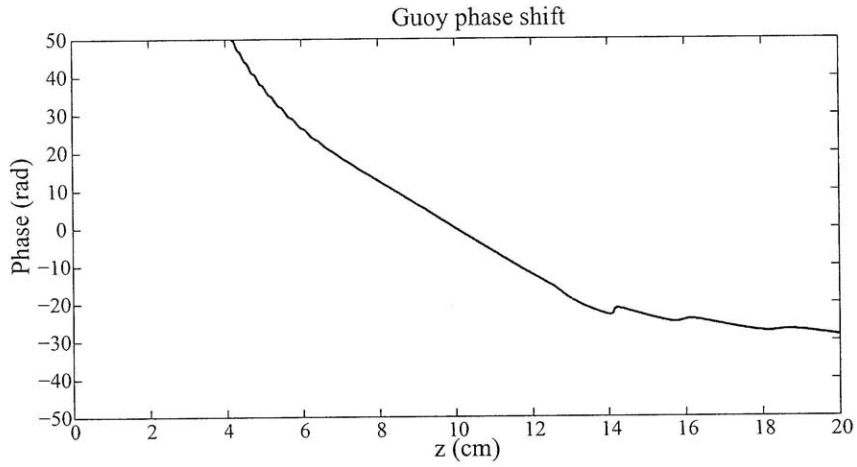

Figure 4-24: Guoy phase shift calculated numerically.

The Guoy phase shift is referred to the fundamental field, so when it is considered in the context of the generation of the nth harmonic the effective phase slip in terms of the harmonic wave gets multiplied by n. Also, for the presented cavity it is not well defined outside of the focus, since the field is practically zero on the z-axis in proximity of the mirrors.

The second predominant phase effect is due to the phase of the atomic dipole (see section 2.3). In this case, the slopes reported are correct when the ponderomotive energy is expressed in atomic units with $\omega_0 = 1$.

Given the ponderomotive energy in SI units in terms of the intensity,

$$U_p^{(S.I.)} = \frac{e^2 Z_0}{2 m_e \omega_0^2} I,$$

it can be easily converted into renormalized atomic units[16] as

$$U_p^{(a.u.)} \approx \frac{U_p^{(S.I.)}}{4.36 \times 10^{-18} \cdot \omega_{a.u.}},$$

where the frequency in atomic units is $\omega_{a.u.} = 24.2 \times 10^{-18}\omega$.

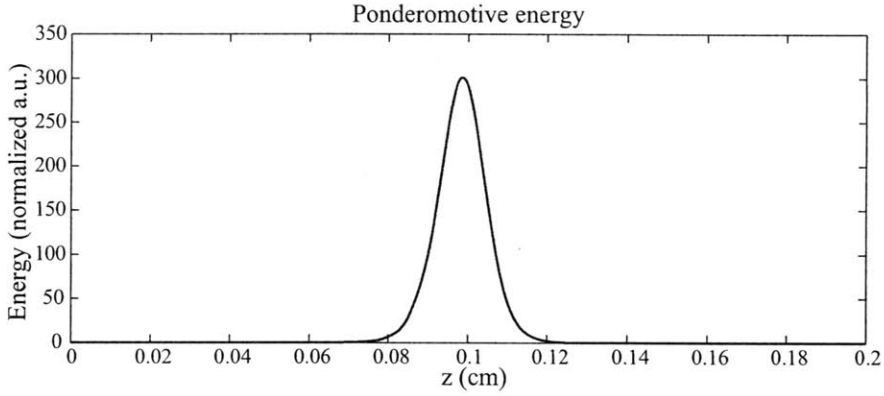

Figure 4-25: Ponderomotive energy in normalized atomic units.

The ponderomotive energy along the z-axis for the cavity above is shown in figure 4-25 for a peak intensity of 5×10^{14} W/cm^2. Consider the 101^{st} harmonic, at $\lambda \approx 20$ nm. In that case, the cutoff occurs for $U_p = 31.5$ in normalized atomic units, so from the figure we can see that we are above that intensity for the most part of the focus.

The total phase shift between the fundamental and the harmonic can be computed, and it is shown in figure 4-26. The linear phase due to the focus characteristics becomes very steep due to high harmonic order, and the dipole phase shift creates a visible *dip* in the curve, creating two regions in which the phase shift has zero rate of change. Observing the one closer to the peak of intensity (i.e. the local minimum), we can see that the generation of the 101^{st} harmonic can occur over a region spanning about 500 μm.

If the phase shift for a higher harmonic is analyzed, in this case the 281^{st}, shown in figure 4-27, the Guoy phase shift is much more dominant, moving the two phase-

[16]Here we care only about the numerical value. Assume that appropriate multiplicative constants are applied so that the final unit for phase is the radian.

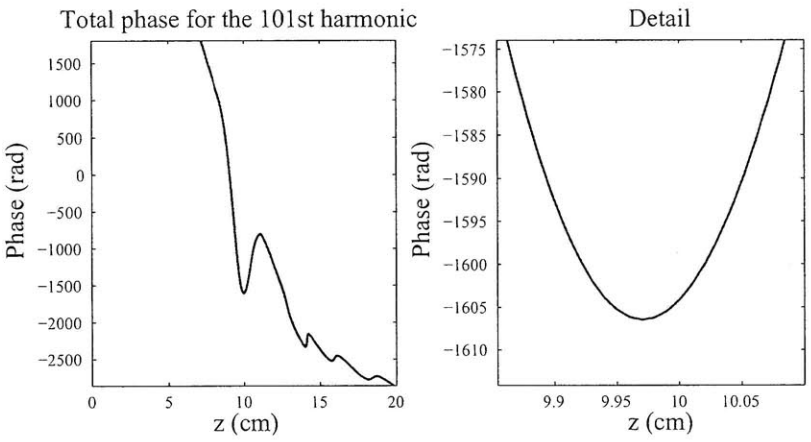

Figure 4-26: Total phase shift for the 101^{st} harmonic.

matched regions closer to each other, and increasing the length over which the nonlinear generation is coherent. In this case, the process can be phase matched for slightly over 1 mm.

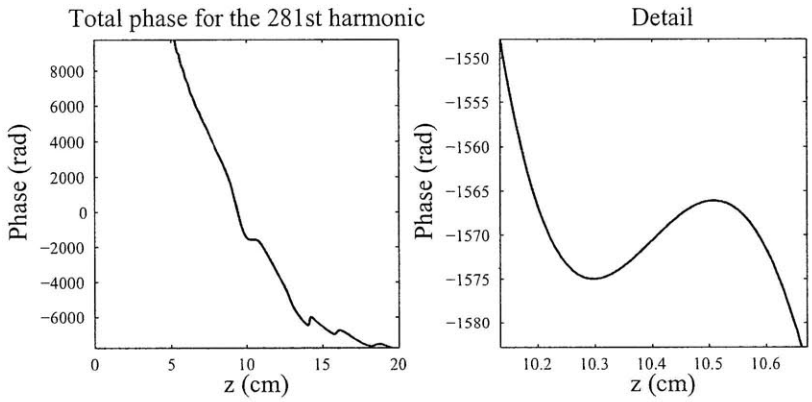

Figure 4-27: Total phase shift for the 281^{st} harmonic.

Unfortunately, as higher harmonics are generated, the phase matched regions shift, so it is unlikely that the entire spectrum of harmonics can be generated without destructive interference.

There are a few remedies to this problem. First of all, it is possible to increase the size of the cavity. In the example considered, the intensity is enough to generate harmonics up to the 1000^{th} order, but the phase of the focus limits phasematched emission to approximately the 300^{th} order. If the ring radius is increased by a factor

of $\sqrt{3}$ and the cavity length by a factor of 3, so to maintain the same gain, the slope of the Gouy phase will be reduced by a factor of 3, allowing to generate all the harmonics up to around the 1000^{th} order at the expense of increasing the pulse energy by a factor of 3 as well (in which case though the area of the focus and so the harmonic power output goes up by the same factor).

Another possibility is to increase the intensity, so that the dipole phase will have a dominant effect for more harmonics. This solutions reduces the length where the interaction is phasematched, but increases the overlap of the phasematched regions for different harmonics (starting from the lower orders).

It is important to point out that for most applications it is not necessary to have the entire spectrum of harmonics, and this cavity still allows for generation of octave spanning high harmonic spectra while phase matched, if the gas jet location and thickness is determined correctly.

Chapter 5

Experimental work

To confirm experimentally the viability of the proposed cavity, I attempted to implement the system outlined in section 4.4. Unfortunately, the unusual substrate prevented me from using the semiconductor fabrication facilities, and getting trained in a laboratory with the necessary capabilities was not a possibility before the end of this work, therefore the full cavity has not been completed. However, the experimental work done so far shows that the ring mirrors are fairly simple to create.

5.1 Fabrication of the mirrors

The system shown in section 4.4 was the model for a possible system to implement. The 633 nm design wavelength was chosen due to the availability of He-Ne gas lasers, and the fact that operating with visible light would be simpler for alignment and observation for a novel cavity design.

The mirrors of choice were the PR1-633-99-0537-0.15CC from CVI Lasers (Albuquerque, NM), which are dielectric mirrors with a power reflectance between 98.5% and 99.5%. The average radius of the ring was chosen to be 1.3 mm because of the 15 cm curvature and the availability of axicons with 175° cone angle.

The idea is to deposit a layer of positive resist (S1813) on top of the dielectric stack, and expose it with a mask shaped like the ring. The fact that the mirrors are concave is not a problem both for spinning the resist and for the lithography step,

since even with a curvature of 15 cm a 1/2 inch mirror goes only about 130 μm below the rim level. Using a 400 nm light source, the ring has to be oversized by less than 10 μm on the mask.

The mask was created with an imagesetter on film (Printworks, Cambridge, MA), and was fixed on a glass slide which was balanced on the mirror's outer rim, keeping the emulsion side on the bottom.

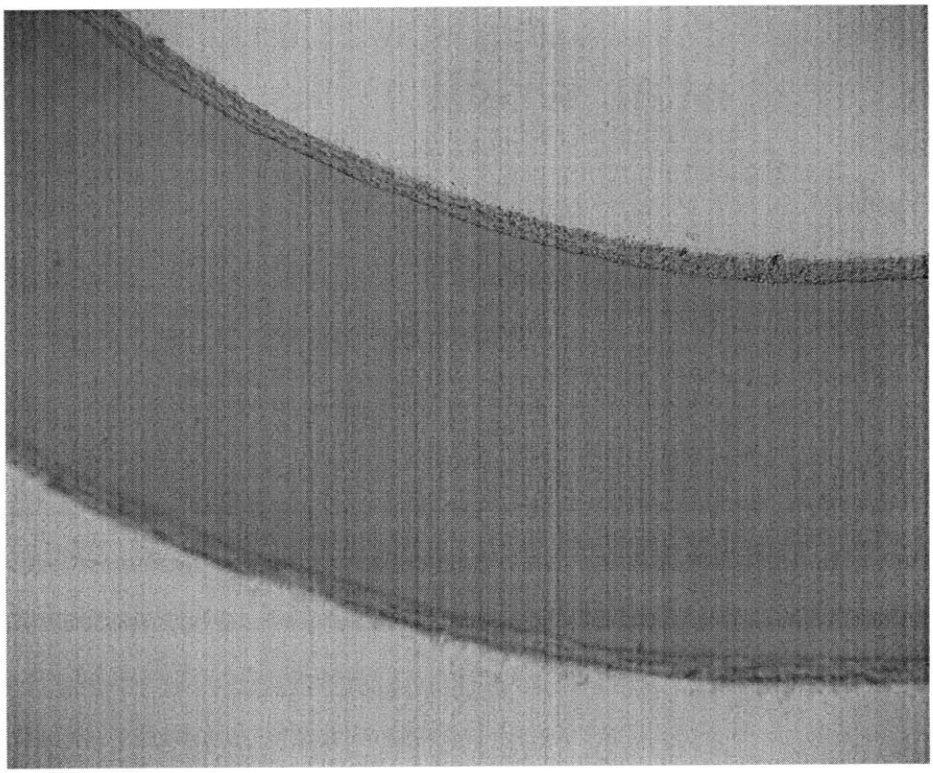

Figure 5-1: Etched mirror.

The mirror shown in figure 5-1 has been etched using an ammonium fluoride/potassium fluoride etching paste. While the border is rough for approximately 25 μm, the portion that is preserved is quite circular and precise. Etching in HF will produce much better results, but it has not been possible in time for this work.

5.2 Monochromatic cavity stabilization

If the mirrors reflect 99% of the power, the width of a transverse cavity resonance will be approximately 1 nm, therefore the optical separation between the mirrors should

be stable within 1 Å of a resonance. It is impossible to achieve this kind of stability purely passively, therefore a feedback system was developed to control one of the cavity mirrors, moved by a piezo stack.

The control signal was supplemented with a high frequency sinusoidal signal (10 kHz) which produced small oscillations around the operating point. A photodetector collected the output of the second mirror, and the output signal was used to measure the small signal gain at the operating point by homodyne detection of the 10 kHz signal. The local small signal gain (i.e. the gain of the HF signal) is proportional to the slope of the resonance peak, and in particular will be zero at the maximum, and vary linearly around it.

Using the small signal gain as the error signal, it is possible to stabilize the cavity with a lead compensator. The stabilized cavity was tested successfully with higher reflectance mirrors, which produced resonant peaks about 2.5 Å wide, so this simple stabilization scheme is able to keep the optical pathlength between the mirrors stable to within a fraction of an angstrom.

By operating the cavity off confocal, it was possible to separate and photograph the Laguerre-gaussian modes, shown in figure 5-2. Slight angular variations are due to the fact the some high-order angular modes get excited due to the alignment which is not perfect. The distortion of the pattern is due to perspective, since the camera was capturing the scene at an angle.

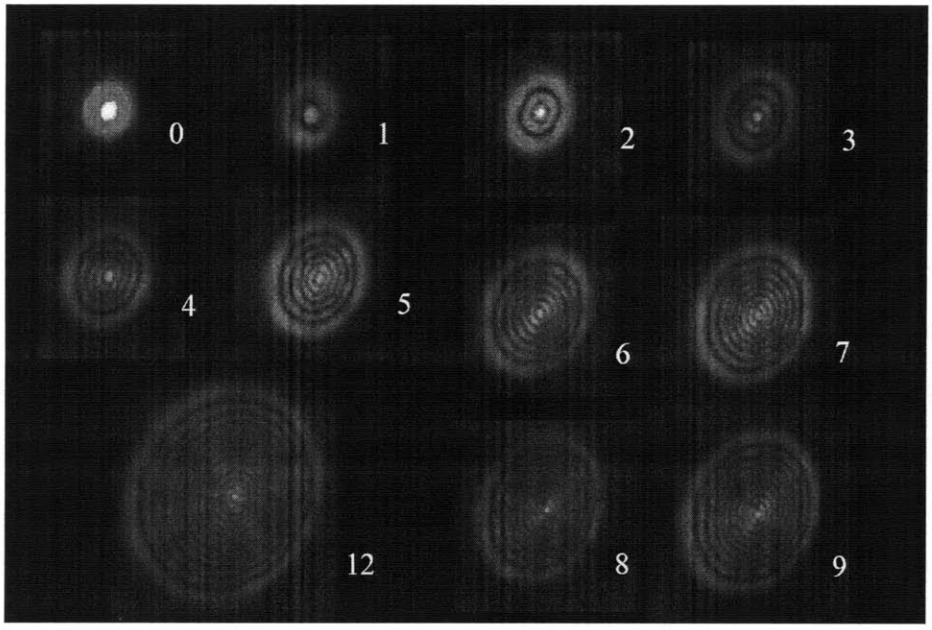

Figure 5-2: Pictures of the $LG_{0,0}$ to $LG_{9,0}$ and $LG_{12,0}$ modes.

Chapter 6

Conclusions

The proposed cavity design appears to be very promising when applied to HHG. The power enhancement offered by the resonator, together with the very high intensity gain from the mirrors to the focus, provide a practical way to create pulses in the intensity regime needed for HHG without the need of additional amplification.

While some aspects have not been taken in consideration in this work, such as a way of introducing the gas jet in the middle of the mode and the effects due to perturbative nonlinearities, it appears that they should not pose a major problem in the realization of such a system.

Despite the unusual mode shape, it is possible to achieve coupling efficiencies of more than 50% from a standard gaussian beam by using a fairly simple optical setup. The theoretical expressions derived for the size of the mirrors required for high gain and single mode operation show that the required system size is quite small. Furthermore, I demonstrated a practical way to construct the needed mirrors.

The phase matching considerations suggest that it is possible to generate octave spanning frequency combs in the EUV and soft X-ray region of the spectrum, with immediate applications in frequency metrology and in the generation of attosecond pulses.

Aside from HHG, this cavity is able to create a really intense light field from relatively inexpensive sources, and so it could find other uses in the case where strong fields are requires, such as in laser electron acceleration.

Bibliography

[1] Maciej Lewenstein, Pascal Salières, and Anne L'Huillier. Phase of the atomic polarization in high-order harmonic generation. *Phys. Rev. A*, 52(6):4747–4754, Dec 1995.

[2] P. A. Franken, A. E. Hill, C. W. Peters, and G. Weinreich. Generation of optical harmonics. *Phys. Rev. Lett.*, 7(4):118–119, July 1961.

[3] M. Ferray, A. L'Huillier, X. F. Li, L. A. Lompre, G. Mainfray, and C. Manus. Multiple-harmonic conversion of 1064 nm radiation in rare gases. *J. Phys. B: At. Mol. Opt. Phys.*, 21(3):31–35, February 1988.

[4] E. Goulielmakis, M. Schultze, M. Hofstetter, V. S. Yakovlev, J. Gagnon, M. Uiberacker, A. L. Aquila, E. M. Gullikson, D. T. Attwood, R. Kienberger, F. Krausz, and U. Kleineberg. Single-cycle nonlinear optics. *Science*, 320:1614, 2008.

[5] J. Itatani, J. Levesque, D. Zeidler, Hiromichi Niikura, H. Pépin, J. C. Kieffer, P. B. Corkum1, and D. M. Villeneuve. Tomographic imaging of molecular orbitals. *Nature*, 432:867–871, December 2004.

[6] A. Ashkin, G. Boyd, and J. Dziedzic. Resonant optical second harmonic generation and mixing. *Quantum Electronics, IEEE Journal of*, 2(6):109–124, June 1966.

[7] R. Jason Jones, Kevin D. Moll, Michael J. Thorpe, and Jun Ye. Phase-coherent frequency combs in the vacuum ultraviolet via high-harmonic generation inside a femtosecond enhancement cavity. *Phys. Rev. Lett.*, 94(19):193201, May 2005.

[8] D. C. Yost, T. R. Schibli, and Jun Ye. Efficient output coupling of intracavity high-harmonic generation. *Opt. Lett.*, 33(10):1099–1101, 2008.

[9] Kevin D. Moll, R. Jason Jones, and Jun Ye. Output coupling methods for cavity-based high-harmonic generation. *Opt. Express*, 14(18):8189–8197, 2006.

[10] Hermann A. Haus. *Waves and fields in optoelectronics*, chapters 1 and 4. Prentice-Hall, Englewood Cliffs, New Jersey, 1984.

[11] Joseph W. Goodman. *Introduction to Fourier optics*, chapter 2. Roberts and Company, Englewood, Colorado, third edition, 2004.

[12] Hermann A. Haus. *Waves and fields in optoelectronics*, chapter 5. Prentice-Hall, Englewood Cliffs, New Jersey, 1984.

[13] D. Auston. Transverse mode locking. *Quantum Electronics, IEEE Journal of*, 4(5):372–372, May 1968.

[14] I. Kimel and L.R. Elias. Relations between hermite and laguerre gaussian modes. *Quantum Electronics, IEEE Journal of*, 29(9):2562–2567, Sep 1993.

[15] Gilberto Abram. Femtosecond enhancement cavities with apertures for efficient high power euv generation using high harmonics. Undergraduate Advanced Project, MIT, June 2008.

[16] Li Yu, Meichun Huang, Mouzhi Chen, Wenzhong Chen, Wenda Huang, and Zhizhong Zhu. Quasi-discrete hankel transform. *Opt. Lett.*, 23(6):409–411, 1998.

[17] Manuel Guizar-Sicairos and Julio C. Gutiérrez-Vega. Computation of quasi-discrete hankel transforms of integer order for propagating optical wave fields. *J. Opt. Soc. Am. A*, 21(1):53–58, 2004.